A molecular circuit regulates fate plasticity in emerging and adult AT2 cells

Amitoj S Sawhney[1#], Brian J Deskin[2#], Junming Cai[1], Daniel Gibbard[1], Gibran Ali[1], Annika Utoft[1], Xianmei Qi[1], Aaron Olson[1], Hannah Hausman[1], Liberty Sabol[1], Shannon Holmberg[1], Ria Shah[1], Rachel Warren[1], Stijn De Langhe[1], Rui Benedito[5], Zintis Inde[2,3], Kristopher A Sarosiek[2,3], Evan Lemire[2], Adam L Haber[2], Liu Wang[4], Zong Wei[4], and Douglas G Brownfield[1,2+]*

[1]Division of Pulmonary and Critical Care Medicine, Department of Medicine, Mayo Clinic College of Medicine and Science, Rochester, MN 55905, USA

[2] Molecular and Integrative Physiological Sciences Program, Harvard T.H. Chan School of Public Health, Boston, MA, USA

[3]John B. Little Center for Radiation Sciences, Harvard T.H. Chan School of Public Health, Boston, MA, USA

[4]Department of Physiology and Biomedical Engineering, Mayo Clinic College of Medicine and Science, Scottsdale, AZ 85259, USA.

[5]Molecular Genetics of Angiogenesis Group, Centro Nacional de Investigaciones Cardiovasculares (CNIC), Madrid E28029, Spain

# These authors contributed equally to this work.
[+] Current address: Division of Pulmonary and Critical Care Medicine, Departments of Physiology and Biomedical Engineering and of Biochemistry and Molecular Biology, Mayo Clinic College of Medicine and Science, Rochester, MN 55905

* Corresponding author. Email: brownfield.douglas@mayo.edu

Abstract

Alveolar AT1 and AT2 cells are vital for lung gas exchange and become compromised in several diseases. While key differentiation signals are known, their emergence and fate plasticity are unclear. Here we show in the embryonic lung that single AT2s emerge at intermediate zones, extrude, and connect with nearby epithelium via interlumenal junctioning. We observe that AT2s retain fate plasticity until the bZIP transcription factor C/EBPα suppresses Notch signaling at a novel *Dlk1* enhancer. Both *Dlk1* and *Cebpa* are regulated by the polycomb repressive complex (PRC2), which together form a "pulse generator" circuit that times *Dlk1* expression and thus Notch activation, resulting in a "salt and pepper" pattern of AT1 and AT2 fate. In injured adult lungs, C/EBPα downregulation is required to re-access AT2 fate plasticity and is mediated by the dominant negative C/EBP family member CHOP. Finally, *Cebpa* loss also activates a "defender" AT2 state, distinct from its reparative state, and we propose AT2s toggle between either state following infection to protect and repair alveoli.

44 **Introduction**

45 Alveoli are the sites of gas exchange in the lung that are lined by two distinct epithelial cell
46 types. The flat surface of alveolar type 1 (AT1) cells facilitates gas exchange while cuboidal
47 alveolar type 2 (AT2) cells secrete surfactant to prevent alveolar collapse. Defective alveoli
48 underly several maladies—bronchopulmonary dysplasia (BPD) in infants, chronic obstructive
49 pulmonary disease (COPD)/emphysema[1], pulmonary fibrosis[2], lung adenocarcinoma[3, 4], and
50 respiratory infections like Severe Acute Respiratory Syndrome (SARS)[5, 6] and COVID-19[7].
51 Deciphering how these crucial alveolar cell types emerge as well as the mechanisms that regulate
52 their fate is imperative for developing therapies that will not only slow or stop disease
53 progression but may even promote lung repair.

54 As alveologenesis begins, AT1 and AT2 cells arise from a common pool of distal
55 progenitors (DP)[4, 8, 9, 10, 11], with differentiation detected as early as embryonic day 16.5 (e16.5)
56 in mice, save for one study reporting an earlier timepoint[12]. Upon differentiation, AT1 and AT2
57 cells are arranged in a salt and pepper pattern[13] along a lumenal surface which, as alveoli mature,
58 interconnect with lumens of anatomically distinct branches to facilitate gas conduction between
59 alveoli[14]. After development, mature AT2 cells can act as antigen presenting cells in an immune
60 response[15, 16] (partly directed interferon signaling[17, 18]), as well as facultative stem cells following
61 injury[4, 11, 19, 20 21] (directed by Wnt[22] and Notch[23] signaling). While both AT2 states are critical
62 after infection for alveolar recovery, a recent study found interferon stimulation suppresses repair
63 of the lung epithelium following infection[24, 25], suggesting that signals driving these states may
64 oppose one another at the cellular level.

65 Here we show nascent AT2 cells are first detected molecularly at e15.5 as singletons at
66 stereotyped intermediate regions of distal branches. Following basal extrusion, we observe

67 nascent AT2s can form *de novo* attachments to nearby but anatomically separate epithelia, a step
68 that is likely critical in stitching together alveolar lumen and that we term "interlumenal
69 junctioning", followed by sporadically patterned AT2 maturation, distinct from the "proximal-to-
70 distal wave" pattern known to initiate differentiation of AT1s and AT2s earlier[13].

71 We determine that nascent AT2s retain fate plasticity into the first perinatal week,
72 revising the lineage model to include a "window of fate plasticity" spanning from distal
73 progenitors to the AT2 lineage. From screening transcriptional regulators around this window,
74 we identify a critical negative regulator of AT2 fate plasticity, the bZIP transcription factor
75 C/EBPα, that when lost results in AT2-to-AT1 conversion. Previously C/EBPα has been reported
76 to play a role in epithelial homeostasis[26] and is implicated in fate regulation in multiple tissues,
77 including the blood and liver[27]. Further, we found that the observed AT2-to-AT1 differentiation
78 was mediated in a non-cell autonomous manner by the Notch regulator DLK1, a cell-surface
79 transmembrane protein[28] that has been associated with brain and muscle development, stem cell
80 maintenance, lung cancer, and abnormal tissue repair[23, 29]. Observing a pulsed expression of *Dlk1*
81 during alveologenesis, we find *Dlk1* and *Cebpa* are both regulated by the polycomb repressive
82 complex (PRC2), and determine these components together constitute an incoherent feed
83 forward loop. Upon abrogation of this "pulsed generator" circuit, we observe a disruption of
84 AT1/AT2 differentiation. PRC2 is a well-established transcriptional repressor that has been
85 shown to regulate DLK1 expression in neuronal fate selection[30] and recent evidence suggests it
86 also modulates C/EBPα expression in the context of adipocyte differentiation[31].

87 Following injury in the adult lung C/EBPα must be downregulated in AT2s for
88 conversion to AT1. We identify that the dominant negative member of the C/EBP family,
89 CHOP, is induced in AT2s following injury and its upregulation promotes AT2-to-AT1

differentiation. Finally, we observe *Cebpa* loss also activates a "defensive" AT2 state that is enriched in antipathogen response genes, likely regulated by interferon signaling, and is mutually exclusive from the AT1-associated DATP state[32].

Results

Timing and pattern of AT2 cell emergence

To delineate newly forming AT2 cells from distal progenitors and their mature counterparts, we analyzed scRNAseq data of the distal epithelial lineage from a prior study sampling the embryonic, perinatal, and adult timepoints of mouse lung development[33] (Fig. 1a). Clustering analysis of the distal epithelium identified both DP and AT1 populations, as well as stratified AT2s into two groups (Fig. 1b) that are also largely separate in time (Fig. 1c). While these AT2 groups positively correlate in gene expression (Pearson coefficient = 0.6, Suppl. Fig. 1a), their distinction as a separate cluster was confirmed by co-assignment probability (Suppl. Fig. 1b). Taken together with the temporal pattern, we refer to the earlier cluster as the nascent AT2 (nAT2) state, and the later as the mature AT2 (mAT2) state. From this distinction, we were able to identify hundreds of genes unique to either DP, nAT2, or mAT2 cluster (Fig. 1d, Suppl. Fig. 1c, and Suppl. Table 2), and initially focused on two for protein-level validation: *Retnla* expressed by nAT2s and *Cd74* by mAT2s (Fig. 1e, Suppl. Fig. 1d). *Retnla* encodes a regulator of inflammation, resistin-like molecule (RELM) α, while CD74 is critical in MHC-II antigen processing. In contrast to commonly used markers that label both DP and AT2 lineage starting around e17.5 (such as SFTPC)[4, 10], RELMα uniquely labels nAT2s at this stage and can be used to distinguish them from both DPs and AT1s, as can be seen at an e17.5 transition zone where the mAT2 marker CD74 is not highly expressed (Fig. 1f, Suppl. Fig. 1e). Further, flow

113 cytometry confirmed at e18.5 that a substantial proportion of marker-expressing AT2s are
114 RELMα^{+} CD74^{-} (Suppl. Fig. 1g), which shifts to RELMα^{-} CD74^{+} in adult AT2s (Suppl. Fig. 1h).
115 Given the distinct labeling of nAT2s by RELMα in the embryonic lung, we used it to
116 identify when and where AT2 cells first emerge during alveologenesis. Careful immunostaining
117 revealed nAT2s emerge as early as e15.5 (Fig. 1g), which steadily increases over time (Fig. 1h).
118 At first emergence, SOX9^{low}/RELMα^{+} and nAT2s are singletons (Suppl. Fig. 1e, f) with retained
119 columnar morphology (Fig. 1i) positioned at anatomical intermediate zones, located between
120 airway smooth muscle (ASM)-covered distal branch stalks and terminal end buds (Fig. 1g,
121 asterisks). After their initial emergence, nAT2s next arise (~e17.5) within distal stalks following
122 ASM to myofibroblast remodeling as previously reported[34], then finally at terminal end buds
123 soon after birth[4]. These observations support a sequential, three zone model of AT2
124 differentiation (Fig. 1j, left, Suppl. Fig. 1d, e) that integrates previously conflicting findings that
125 reported AT2 differentiation first occurring either at terminal end buds[12] or in a proximal-to-
126 distal pattern[4, 9].
127

128 **Nascent AT2s junction with nearby but anatomically distinct epithelium**

129 While imaging RELMα at these timepoints, we also observed nAT2s forming connections to
130 lumens across anatomically separate branches (Fig. 2a), a behavior which increased in frequency
131 over time (Fig. 2b). While it is known that during alveolar maturation AT2 cells are capable of
132 simultaneously integrating into lumens of multiple alveoli[14, 34], the process by which it occurs
133 has yet to be described. Careful immunostaining of junctioning nAT2s revealed their negativity
134 for AT1 markers (PDPN, RAGE, and HOPX) and positivity for AT2 markers (SFTPC, LAMP1,
135 and MUC1) that is often higher than non-junctioned AT2s, suggesting they may be further along

136 in differentiation (Suppl. Fig. 2a, b). Using high resolution imaging and 3D reconstruction, we
137 observed that junctions occurred either directly with the second lumen, or indirectly by
138 attachment to another extruded nAT2 (Fig. 2c, Suppl. Fig. 2c, Suppl. Video 1-4).

139 To further investigate the dynamics of nAT2 junctioning, we performed timelapse
140 confocal microscopy on Precision Cut Lung Slices (PCLS) isolated from e17.5 murine lungs
141 wherein the distal lung epithelium was labeled with a membrane tethered GFP (*Tg*$^{Nkx2.1\text{-}Cre}$
142 *Rosa26*^{mTmG}) wherein nAT2s could be readily visualized to extrude and junction (Fig. 2d). We
143 observed both types of nAT2 junctioning - direct when the interstitial distance was short (Fig.
144 2e) and indirect when greater than a cell length away (Fig. 2f, Suppl. Fig. 2d, Suppl. Video 5).
145 Finally, we observed for most, if not all junctioning nAT2s, a significant reduction in length of
146 MUC1 domains indicative of apical constriction (Fig. 2g, h). Taken together, we believe our
147 observations are of an initial "interlumenal junctioning" event critical in the process of
148 integrating alveolar lumenal surfaces (Fig. 2i, j) that relies upon basal extrusion of nAT2s to
149 junction. Further, we hypothesize the manner of junctioning (direct or indirect) is dependent on
150 interstitial distance, and that defective nAT2 junctioning could result in alveolar simplification
151 similar to what is observed in BPD and COPD.

152

153 **Nascent and mature AT2 state differ in fate plasticity and BH3 regulation.**

154 Following their initial specification, nAT2s undergo maturation in the first week or so after birth,
155 which can be observed by the switch from RELMα to CD74 expression (Fig. 3a, b). As RELMα
156 expression is lost in mAT2s, we observe its concomitant upregulation in the airway epithelium
157 (Suppl. Fig. 3a). In contrast to the initial proximal-to-distal wave pattern that AT1/AT2 fate
158 selection is reported to occur[4, 13], we observe AT2 maturation does not follow this pattern but

159 rather occurs in a sporadic salt-and-pepper pattern (Fig. 3c, d, Suppl. Fig. 3b), suggesting
160 maturation may be governed by a distinct mechanism.

161 Given the molecular distinction between nAT2 and mAT2 states, we next sought to
162 determine whether functional differences also exist. One manner in which time-dependent cell
163 states can vary is in fate plasticity, as has been observed in neutrophils[35] in vivo and lung
164 epithelial iPSCs[36] in culture. To determine whether and how nAT2s and mAT2s differ in fate
165 plasticity, we analyzed two previously generated scRNAseq datasets that sample timepoints
166 either during[12] (Fig. 3e - g, Suppl. Fig. 3c - g) or far beyond[37] (Fig. 3h - j) alveolar epithelial
167 differentiation. Analyzing first the distal epithelium prior to (e15.5) and during (e17.5) alveolar
168 epithelial differentiation, we performed standard clustering as well as UMAP visualization and
169 found that distal epithelial cells isolated from these timepoints only rarely co-clustered (Suppl.
170 Fig. 3e), indicating no e15.5 progenitor population had significantly adopted either AT1 or AT2
171 transcriptional program, a central tenet of the early lineage specification model proposed in a
172 prior study[12] . A weak correlation between one of the e15.5 progenitor clusters (DE3) and the
173 e17.5 progenitor cluster (0.42) was observed (Suppl. Fig. 3e, yellow box), suggesting a shared
174 transcriptional program.

175 Single-cell transcriptional dynamics analysis was next analyzed to determine when and
176 how the AT1 and nAT2s clusters segregate. Performing pseudotime (Suppl. Fig. 3f), velocity
177 (Suppl. Fig. 3g), as well as integrated PAGA-Velocity analysis (Fig. 3e) all identified e15.5
178 clusters as the starting timepoint, as well as identified the AT1 cluster as the predicted endpoint
179 (Suppl. Fig. 3f, g). Further, velocity analysis found a substantial proportion of nAT2s to be on a
180 transcriptional trajectory towards the AT1 cluster, suggesting fate plasticity was retained (Fig.
181 3e, red arrow). To determine whether a subset of nAT2s displayed a biased trajectory towards

182 AT1 differentiation, we established an AT1 and AT2 score based on well-established marker
183 genes[9] and observed a clear stratification within the nAT2 cluster (Fig. 3f). Separating the nAT2
184 cluster by this ratio into two subgroups (High AT1 or Low AT1 gene expression, > 0.5 = High
185 AT1/AT2 score), we compared velocity trajectories and observed a clear separation (Fig. 3g),
186 indicating nAT2 subset with a high AT1/AT2 ratio are leaving the nAT2 state and transitioning
187 to AT1.

188 After observing that embryonic nAT2s possibly retain fate plasticity, we sought to
189 determine how long AT2s retain fate plasticity after birth. Using a previously reported dataset
190 that samples across the lifetime of the distal epithelium of the mouse lung[37], we performed
191 similar processing as before to remove duplicates and non-distal epithelial cells before
192 performing UMAP visualization and clustering analysis (Fig. 3h, i). Analyzing more widely over
193 time, we again observed earlier progenitor populations, mature AT1 and AT2 clusters, as well as
194 a cluster transitioning between them as previously reported[37]. Velocity analysis of this
195 intermediate cluster found the cellular trajectories are oriented away from AT2 and towards AT1
196 (Fig. 3i, red box) like our prior observation. Finally, analysis of the timepoints of cells within the
197 AT2→AT1 transitioning clusters revealed most were from the early perinatal period, suggesting
198 fate plasticity was lost as AT2s mature within the first week after birth (Fig. 3j). To confirm this,
199 we performed alveolosphere differentiation assays following our previously described protocol[10]
200 and found that both nAT2s as well as early mAT2s (PN3) could give rise to AT1 cells (Fig. 3k,
201 l), confirming fate plasticity was lost primarily in a time-dependent manner, independent of
202 nAT2 or mAT2 state. Taken together, our analysis indicates that fate plasticity, a property of
203 DPs, is retained in newly formed AT2 cells for a period of 1-2 weeks after birth, revising the
204 model of the alveolar epithelial fate selection model to include a window of plasticity (Fig. 3m).

205 Another property known to vary from early life to maturity is mitochondrial sensitivity to
206 apoptotic stimuli (apoptotic priming)[38], which is reduced during maturation in several organs but
207 can be retained in certain stem cell populations[39, 40]. To determine whether apoptotic sensitivity
208 is retained in nAT2s, BH3 profiling was performed on isolated DPs, nAT2s, as well as adult
209 mAT2s. As expected, DPs and nAT2s exhibited heightened sensitivity to pro-apoptotic BH3
210 peptides as indicated by higher rates of cytochrome c release, while mAT2s were largely
211 unresponsive (Suppl. Fig. 3h). Taken together, our findings indicate the nAT2 state retains both
212 fate plasticity as well as sensitivity to BH3 regulated apoptosis despite being functionally
213 differentiated.
214

215 **C/EBPα is required to maintain but not select AT2 fate**

216 Given the loss of fate plasticity as nAT2s mature into mAT2s, we next sought to determine how
217 this paradigm is regulated. Referencing the scRNAseq data we previously used to distinguish
218 nAT2 and mAT2 clusters (Fig. 1a, b) as well as AT2s sequenced more deeply by the Tabula
219 Muris Consortium[41], we screened putative transcriptional and epigenetic regulators from a
220 curated list (1,678 genes) and identified 67 genes with ≥ 2-fold enrichment along the AT2
221 (Suppl. Table 3) lineage (DP→nAT2→mAT2) compared to AT1 (Fig. 4a). Of these, we then
222 considered only the 32 genes with known embryonic lethal or lung defects when knocked out in
223 mice (Fig. 4a, Suppl. Fig. 4a). These genes can be stratified into four categories based on
224 expression pattern over time: constitutive, DP-restrictive, DP/nAT2-restrictive, and
225 nAT2/mAT2-restrictive (Fig. 4a, lower and Suppl. Fig. 4a). Of these, we focused on genes
226 expressed in the observed window of fate plasticity (Suppl. Fig. 4b), which narrowed the list to
227 four genes, *Etv5* and *Elf5* (constitutive) as well as, *Cebpa* and *Nupr1* (nAT2/mAT2-Restrictive)

228 (Fig. 4b). While both constitutively expressed genes (*Etv5* and *Elf5*) have been investigated in
229 the lung, findings suggest regulatory roles other than fate plasticity, as ETV5 is required
230 primarily to maintain AT2 survival[42] while ELF5 appears to broadly regulate aspects of lung
231 epithelial differentiation[43]. Further, we excluded study of *Nupr1* given its primary role is in death
232 regulation, not differentiation[44, 45]. This left *Cebpa* as the putative regulator, for which we
233 validated the timing of expression via immunostaining in the embryonic lung (Fig. 4c).

234 Previous *Cebpa* research in the developing mouse lung performed knockouts via a Tet-
235 On approach and concluded it was required for alveolar epithelial differentiation[46, 47]. These
236 findings are conflicting with the expression pattern of *Cebpa*, which is first expressed after AT2
237 differentiation, not before (Fig. 4b, c, Suppl. Fig. 6b). Given this discrepancy, as well as a
238 subsequent study that questioned the viability of the prior Tet-On approach in the lung[48], we first
239 sought to confirm whether *Cebpa* was required for alveolar epithelial differentiation via a more
240 refined method of gene deletion. Using a lineage labeling with efficient recombination approach
241 (*Nkx2.1-Cre*; *Rosa26*$^{mTmG/mTmG}$; *Cebpa*$^{fl/fl}$) wherein distal bipotent progenitors are both
242 fluorescently labeled and floxed gene recombined[10], we tested whether *Cebpa* loss indeed
243 resulted in suppressed differentiation. Surprisingly, we observed that both AT2 and AT1 fate
244 selection occurred despite the absence of *Cebpa* (Fig. 4d, Suppl. Fig. 4c), both at the molecular
245 and morphological level.

246 As we expected *Cebpa* to play a role later in development consistent to when it is
247 expressed, we next performed sparsely labeling with efficient deletion experiment wherein
248 *Cebpa* was deleted in a subset of AT2 cells starting in the early perinatal period (~PN5, *LyzM*^{Cre};
249 *Rosa26*$^{mTmG/mTmG}$; *Cebpa*$^{fl/fl}$). While lineage-traced control AT2 cells maintain their fate into
250 adulthood, a significant portion of AT2 cells lacking *Cebpa* converted into AT1 cells (Fig. 4e, f),

251 suggesting an increase in AT2 fate plasticity. Finally, we confirmed the result using an AT2-
252 restrictive tamoxifen-inducible Cre recombinase line (*Sftpc*^{CreER}) which again demonstrated an
253 increase in conversion to AT1 fate both morphologically and molecularly (Suppl. Fig. 4d). Taken
254 together, we determined that C/EBPα, a bZIP transcription factor expressed following AT2 cell
255 specification is required during the perinatal period to maintain, not select, AT2 fate, suggesting
256 it plays a role in suppressing fate plasticity during the transition from nascent to mature AT2
257 state.
258

259 **C/EBPα represses a non-cell autonomous AT1 differentiation program driven by DLK1**

260 To determine more precisely how C/EBPα regulates AT2 fate plasticity, we conducted
261 scRNAseq of the alveolar epithelium from both control (*Cebpa*$^{wt/fl}$) and AT2-floxed (*Cebpa*$^{fl/fl}$)
262 lungs, wherein Cre-mediated deletion was induced in the perinatal period using *Sftpc*^{CreER} in
263 combination with the Tg(iSuRe-Cre)[49] allele. Retrospective identification of cell types via
264 Louvain clustering using Seurat was able to distinguish control (AT2 – *Cebpa*$^{wt/fl}$) and *Cebpa*
265 floxed (AT2 – *Cebpa*$^{fl/fl}$) AT2s as well as AT1s (Fig. 5a-i, ii), a subset of which we confirmed
266 were derived from AT2 cells following Cre induction by expression of the Cre-inducible reporter
267 Tg(iSuRe-Cre) (Suppl. Fig. 5a), confirming our prior lineage tracing experiments. We observed a
268 substantial down- and upregulation of 117 and 116 genes respectively upon loss of *Cebpa*
269 (Suppl. Fig. 5b). To determine how AT2 or AT1 gene expression overall during development
270 (Suppl. Fig. 5c) and was impacted following *Cebpa* loss, we first used gene scores to broadly
271 assess changes in either AT2 or AT1 related genes (Suppl. Fig. 5e). While no significant
272 upregulation of AT1 genes was observed (suggesting C/EBPα likely does not repress fate
273 plasticity by directly repressing the AT1 gene program), a reduction in overall AT2 genes was

274 observed in AT2s lacking *Cebpa* (Fig. 5a-ii). To further determine how AT2-associated genes
275 were altered, we separately assessed genes restrictively enriched in either nAT2 or mAT2 state
276 (Suppl. Fig. 5d). Upon *Cebpa* loss, AT2 cells reduce expression of mAT2 genes while
277 concomitantly upregulating nAT2 gene expression (Fig. 5a-ii), suggesting re-accessing of a
278 plastic, nascent-like AT2 state.

279 To better understand the behavior of these plastic AT2s as well as focus our investigation
280 of their molecular regulators, we next sought to determine whether the AT2-to-AT1
281 differentiation observed upon *Cebpa* loss was mediated by a cell autonomous or non-
282 autonomous mechanism. While a common experimental approach in *Drosophila* research[50, 51] to
283 delineate between mechanisms targeting internal signaling or proliferation (cell autonomous)
284 versus expression of an extracellular signal (non-cell autonomous), such experiments are less
285 common in the mouse and have been difficult using inducible Cre lines until the development
286 transgenic alleles such as Tg(iSuRe-Cre) [49]. Usage of a CreER line alone under sparse labeling
287 conditions can result in incomplete or mosaic recombination of alleles and label "escaper
288 cells"[52], confounding interpretations of the gene's necessity. To overcome this, We next
289 performed sparse labeling with efficient *Cebpa* deletion using the Tg(iSuRe-Cre) allele
290 (*Sftpc*^{CreER}*; Tg(iSuRe-Cre); Cebpa*$^{fl/fl}$) at a tamoxifen dose we determine labels ~20% of AT2s
291 validated by immunostaining (Fig. 5b, c, Suppl. Fig. 5f, g). This method of sparse labeling with
292 efficient recombination can be used to delineate whether a phenotype is regulated in a cell
293 autonomous (i.e. via a cell intrinsic mechanism, in which case the phenotype would occur in both
294 sparse and non-sparse labeling experiments) and non-cell autonomous programs (i.e. via a cell
295 extrinsic mechanism, in which case the phenotype would occur significantly less if at all in the
296 sparse labeling experiment). In contrast to when *Cebpa* is removed from most AT2s (~99%), we

297 observed that removal of *Cebpa* from sparse numbers of AT2s (~20%) resulted in a substantial
298 reduction of AT2-to-AT1 differentiation as assessed by percentage of lineage labeled AT1s and
299 proliferation (Fig. 5b, Suppl. Fig. 5h). This finding strongly indicates that AT2 fate plasticity acts
300 via a cell non-autonomous mechanism, likely an extracellular signal, to promote AT2-to-AT1
301 differentiation.

302 Given this, we focused our screen on genes upregulated in *Cebpa* deleted AT2s that
303 encode proteins with an extracellular localization (GO:0005615), which returned 22 genes, 6 of
304 which were also expressed in the nAT2s from the prior scRNAseq timecourse, and of these 4 are
305 localized on the cell membrane or secreted (*Dlk1*, *Col23a1*, *Cd14*, and *Apoc1*) (Fig. 5d, Suppl.
306 Fig. 5i, j). The most highly upregulated of these genes is *Dlk1*, which encodes a single pass type
307 I membrane protein localized to the outer cell surface that is known to regulate Notch signaling[53]
308 and AT2-to-AT1 differentiation[23] (Fig. 5d, red).

309 Finally, we confirmed DLK1 is also upregulated at the protein level following *Cebpa* loss
310 in culture (Suppl. Fig. 5k), and further observe its expression is maintained under sparse labeling
311 with efficient *Cebpa* deletion in vivo, suggesting C/EBPα directly regulates DLK1 in a cell
312 autonomous manner (Fig. 5e, f). Taken together, we hypothesize that C/EBPα begins to block
313 fate plasticity of specified AT2s by direct suppression of *Dlk1* and its subsequent activation of
314 Notch signaling.

315 After establishing C/EBPα likely directly represses *Dlk1* expression, we sought to
316 determine where within the genome it is mediated. We performed bulk ATAC-seq on both
317 control and *Cebpa* floxed AT2s in the same experiment timeline as for scRNAseq (Suppl. Fig.
318 5l), but AT2-lineage cells were further purified by FACS using the genetically encoded
319 fluorophore tdTomato. After confirming correlation between ATACseq replicates (Suppl. Fig.

320 5m), we identified 23,764 sites within the genome that significantly changed in accessibility
321 following *Cebpa* loss (Suppl. Fig. 5n), with decreased accessibility associated with 3,986 genes,
322 consistent with C/EBPα's well established role as a positive regulator of gene expression[54]. We
323 observed 369 DEGs shared between our ATACseq and scRNAseq datasets (Suppl. Fig. 5o) and
324 mapped the proportions of genomic features that are up- and downregulated (Suppl. Fig. 5p). We
325 also observed a smaller but substantial number of genes (2,384) with associated upregulation in
326 chromatin accessibility following *Cebpa* loss, indicating repressive regulation, including the
327 transcriptional start site (TSS) of *Dlk1* (Fig. 5g). Further, the change in enrichment of
328 transcription factor binding sites following *Cebpa* loss is consistent with prior work on Nkx2.1
329 and AP-1 acting as a bivalent co-factor to reinforce fate of both AT1 (via Yap/Taz interactions)
330 and AT2 (via C/EBPα) cells[55] (Suppl. Fig. 5q, r, s).

331 In investigating putative regulatory sites near *Dlk1*, we initially considered the nearby
332 intergenic differentially methylated region (IG-DMR) previously demonstrated to strongly
333 regulate *Dlk1* expression[56]. While no change in accessibility was detected in the IG-DMR locus,
334 a region nearby was found to decrease following *Cebpa* loss (Fig. 5g). Further, this region
335 included a predicted regulatory site containing a C/EBPα binding motif (Fig. 5g, dashed red)
336 where it could possibly act to repress *Dlk1* and that we validated C/EBPα binds to in AT2 cells
337 in a previously published ChIPseq dataset[52].

338

339 **PRC2 and C/EBPα act as a *Dlk1* "pulse generator" critical for patterning alveolar**
340 **epithelial fate**

341 Given the perinatal repression of *Dlk1* by C/EBPα, we were curious of its expression earlier in
342 lung development. As previously reported[57, 58], we observed that *Dlk1* is lowly expressed at

343 stages prior to alveolar epithelial differentiation (e12.5-e15.5) both at the protein (Fig. 6a) and
344 RNA level (Fig. 6b, dashed grey box). Further, *Dlk1* expression appeared to peak in the period
345 from e17.5 to PN1 (Fig. 6a, b, Suppl. Fig. 6a). As *Cebpa* is not detected at earlier stages (≤
346 e15.5) (Suppl. Fig. 6b), we were curious how *Dlk1* downregulation is mediated. Suppression of
347 *Dlk1* has also been found to be mediated by the polycomb repressive complex (PRC2), including
348 the H3-K-27 methyltransferase EZH2[59]. We observed that genes encoding PRC2 members were
349 enriched at earlier stages (Fig. 6b, red text), and further that EZH2 protein is substantially
350 downregulated after e16.5 (Fig. 6c).

351 As EZH2 and the PRC2 complex are enriched earlier when *Dlk1* is downregulated, we
352 next tested whether EZH2 activity is required to suppress DLK1 in culture. Isolated e15.5 DPs
353 were cultured as organoids and treated either with FGF7 alone or with the EZH2 inhibitor
354 GSK126 (10 μM) for 4 days (Fig. 6d). While control organoids had detectable DLK1 protein
355 (~12% $DLK1^+$ cells), levels significantly increased when treated with the EZH2 inhibitor (~22%,
356 Fig. 6e), indicating EZH2 methyl transferase activity is required for DLK1 suppression.

357 When characterizing the expression of *Ezh2* alongside *Cebpa*, we noticed a consistent
358 mutually exclusive pattern (Fig. 6b, Suppl. Fig. 6c), suggesting EZH2/PRC2 might also suppress
359 *Cebpa*. We analyzed a published ENCODE epigenetic dataset that mapped the PRC2
360 modification H3K27me3 across development[60] and observed its time-dependent reduction at the
361 *Cebpa* locus concomitant to when *Cebpa* expression is upregulated (Suppl. Fig. 6d). Further,
362 analysis of ChIPseq database of mouse tissues and cells[61] confirmed significant enrichment in
363 binding of EZH2 as well as other PRC2 components near the *Cebpa* locus (Fig. 6f). To
364 determine whether EZH2/PRC2 is also necessary for repressing C/EBPα, we again conducted
365 organotypic culture with e15.5 DPs during which differentiation was promoted by addition of

366 FGF7 as previously described[10]. Blocking of EZH2 activity by GSK126 significantly increased
367 the percentage of C/EBPα^{+} cells compared to control (55% versus 34% respectively, Fig. 6g, h).
368 Finally, we confirmed whether *Ezh2* is required in vivo to suppress C/EBPα by using a sparse
369 deletion approach wherein a Cre line we previously found to sparsely label DPs[10] (*Tg$^{Nkx2.1\text{-}Cre}$*)
370 was bred to a transgenic line to delete *Ezh2* and lineage label by GFP (*Tg$^{Nkx2.1\text{-}Cre}$*
371 *Rosa26$^{mTmG/mTmG}$; Ezh2$^{fl/fl}$*). Immunofluorescence conducted at e15.5, a timepoint where no
372 C/EBPα is observed (Suppl. Fig. 6b), found significant upregulation of C/EBPα in *Ezh2* deleted
373 (GFP^{+}) versus control (RFP^{+}) DPs residing within the same end buds (Fig. 6i, j).
374 The interactions between EZH2/PRC2, C/EBPα, and DLK1 we observed appeared to fit
375 the definition of a type 2 incoherent feed-forward loop[62] (I2-FFL, Fig. 6k). An incoherent
376 feedforward loop (I-FFL) is a type of network motif found in biological systems, such as gene
377 regulatory networks. It contains three components, a regulator, an intermediate , and a target –
378 we propose these components in our model to be PRC2, C/EBPα, and *Dlk1*, respectively (Fig.
379 6k). The term incoherent means that the regulator (PRC2) acts in a conflicting manner to the
380 target — by both inhibiting (directly on *Dlk1*) and activating it (indirectly through repression of
381 the repressive intermediate C/EBPα. One emergent property of an I-FFL is the capacity to
382 generate a pulse of the target gene's expression (*Dlk1*) following downregulation of the upstream
383 regulator (EZH2/PRC2). To more precisely assess whether the observed temporal pattern of
384 *Dlk1* expression matched the pulse predicted by and I2-FFL, we perform modeling using the
385 biocircuits package (https://biocircuits.github.io/). After establishing reasonable values for
386 parameters describing the relationship of factors in the I2-FFL (see Methods), the model was
387 found to fit well to the observed *Dlk1* expression pattern as assessed by root mean squared error
388 (RMSE = 0.12, Fig. 6l, Suppl. Fig. 6e). Next, we wanted to assess the importance of this

389 molecular circuit in patterning alveolar epithelial differentiation. Immunostaining of e15.5 DPs
390 in organotypic culture for markers of AT2 and AT1 fate (SFTPC and RAGE, respectively)
391 revealed that blocking EZH2 activity, with or without FGF7 treatment, significantly increased
392 the proportion of molecularly specified AT2s while concomitantly reducing AT1s compared to
393 FGF7 alone (Fig. 6m, n). Finally, we wanted to assess whether lateral inhibition of Notch
394 signaling occurs in AT1 cells, as it has been well demonstrated to promote a spatial "salt and
395 pepper" pattern of cell fates[63]. Analysis of scRNAseq timecourse datasets found that nascent
396 AT1 cells upregulate the Notch target gene *Hes1* suggesting signaling upregulation as expected
397 from prior studies[64] as well as downregulation of Notch ligands *Jag1* and *Dll4* that is consistent
398 with lateral inhibition of Notch signaling (Suppl. Fig. 6f, g). Further, we also observe in nAT1s
399 changes in Notch regulators that is also consistent with lateral inhibition, specifically
400 downregulation of *Dlk1* and upregulation of *Dlk2* (Suppl. Fig. 6f, g) - the latter has been found to
401 act as a cis-inhibitor of DLK1[65]. Therefore, our findings suggest that the potential model of
402 *Cebpa*-mediated fate regulation is as follows (Fig. 6o): In the *Cebpa*$^{fl/fl}$ background, the AT2 fate
403 plasticity window is reopened, and the pulsing of DLK1 upon the removal of repressors converts
404 a subset of AT2s into Notch signaling sending cells. Through further lateral inhibition, the
405 molecular circuit depicted in Fig. 6k likely contributes to AT1/AT2 patterning during lung
406 development. Taken together, our findings support the model that EZH2/PRC and C/EBPα act as
407 a molecular circuit (specifically an I2-FFL) to generate a DLK1 pulse during late-stage
408 embryogenesis that is critical to patterning the proportion of AT2 and AT1 cells.
409

410 **C/EBPα suppression is required for accessing both reparative and defensive AT2 states**

411 Given the role of C/EBPα in suppressing plasticity in AT2 cells, we sought to determine if and
412 how it is overridden following injury in the adult lung, where AT2s are well established to act as
413 facultative progenitors to regenerate lost AT1 cells[4, 22]. To first determine if C/EBPα
414 downregulation is required following injury in adulthood for AT2-to-AT1 conversion, we
415 infected adult mouse lungs harboring a Cre-dependent fluorescent reporter (*Rosa26*$^{mTmG/mTmG}$)
416 with AAVs targeting AT2 cell expression via a minimal *Sftpc* promoter as previously described[10]
417 to express either Cre alone or Cre and C/EBPα. After five days, we injured lungs via
418 intratracheal instillation of the irreversible FGFR inhibition Fiin1 (14.75 mg/kg, as previously
419 characterized by our group[10]) or intraperitoneal injection of BHT (225 mg/kg) and performed
420 immunostaining 14 days afterwards (Fig. 7a upper, Suppl. Fig. 7a, b). Intratracheal instillation of
421 AAVs efficiently labeled AT2s with high specificity (Suppl. Fig. 7c). While injured lungs
422 showed AT2-to-AT1 conversion when treated with the control AAV, it was significantly reduced
423 in those given C/EBPα overexpressing AAVs (Fig. 7a, b).

424 Next, we examined whether C/EBPα expression is downregulated following injury using
425 the 1X Bleomycin model, which results in patchy regions of injury and that resolve within 4-6
426 weeks. Bleomycin treated lungs were imaged 16 days after administration and injured areas
427 detected by alveolar simplification and reduction in E-cadherin as previously observed[66].
428 Immunostaining for C/EBPα revealed a significant downregulation in injured versus uninjured
429 regions (Fig. 7c, d). This finding is in alignment with analysis of a recent scRNAseq timecourse
430 study[20] following single-dose bleomycin, during which *Cebpa* expression is downregulated in
431 AT2 cells as early as 2 days post bleomycin (Fig. 7e).

432 After establishing the presence and necessity of C/EBPα downregulation following
433 injury, bioinformatic screening of the bleomycin injury timecourse for transcriptional regulators

434 known to suppress C/EBPα that are also upregulated in the previously identified AT2-to-AT1
435 transitionary[20] state (Krt8^{+} ADI, also known as DATP[32] or PATS[67]) identified three genes, *Atf3,*
436 *Atf4,* and *Ddit3* (Fig. 7e, Suppl. Fig. 7e). Both activating transcription factors 3 and 4 are known
437 to bind the *Ddit3* promoter to drive expression[68, 69], and DNA damage-inducible transcript 3
438 protein, also known as C/EBP homologous protein (or CHOP), has been well established to
439 directly bind and act as a dominant negative inhibitor of C/EBP transcription factors[70]. Given its
440 direct interaction and inhibition of C/EBPα, we next wanted to determine whether induction of
441 CHOP is alone sufficient to drive AT2-AT1 conversion. A day after lineage labeling AT2 cells
442 in lungs of perinatal mice (PN11, *Sftpc*^{CreER}*; Rosa26*^{mTmG}), intraperitoneal injections of either
443 vehicle alone or a small molecule inducer of CHOP via PERK activation CCT020312 (2 mg/kg)
444 were administered every four days and lungs isolated at PN25 (Fig. 7f). While little to no lineage
445 labeled AT1s were observed in vehicle treated lungs, there was a significant increase in those
446 treated with CCT020312 (Fig. 7f, g), suggesting PERK/CHOP induction can promote AT2-to-
447 AT1 conversion.

448 To precisely map AT2 transcriptional trajectories and programs following *Cebpa* loss, we
449 conducted Velocity analysis as well as Leiden clustering on our scRNAseq dataset and
450 confirmed a cellular trajectory from AT2 to AT1 cluster as expected (Fig. 7h). Unexpectedly, we
451 observed another distinct trajectory terminating on a distinct AT2 cell cluster that was enriched
452 in genes associated with pathogen defense response and interferon signaling by GO analysis
453 (Fig. 7i, Suppl. Table 2), leading us to name the "defender" state AT2^{def} (Fig. 7h, red).
454 Visualizing the expression of AT2^{def} enriched genes versus those associated with the damage-
455 associated transitionary progenitor (DATP) state[32], we observed these programs were largely
456 mutually exclusive, apparent by both UMAP (Fig. 7j) and SPRING plot (Fig. 7k, l). Given the

457 distinct trajectories, as well as prior research indicating interferon signaling negatively impacts
458 lung epithelial repair[24], we were interested whether stimulation of the AT2^{def} state by interferon
459 signaling would block AT1 conversion in culture. Given the expression pattern of interferon
460 receptors as well as transcriptional targets in the AT2^{def} cluster (Suppl. Fig. 7d, e), we treated
461 cultures with interferon-γ (Fig. 7m). While perinatal AT2s could give rise to AT1s following
462 FGF7 treatment in organotypic culture, addition of exogenous interferon-γ resulted in a
463 significant reduction AT1 conversion, consistent with the model that AT2^{def} and AT2-to-AT1
464 molecular program are antagonistic to each other at the cellular level (Fig. 7m, n). To assess the
465 degree to which these programs are present in the same or separate AT2 cells following injury,
466 we analyzed scRNAseq datasets wherein lungs were injured in distinct ways, including
467 diphtheria toxin ablation of AT1 cells[71], influenza[72], LPS[73], and Bleomycin[20]. In support of our
468 findings following *Cebpa* deletion, DATP and Defender states were found to primarily exist in
469 separate AT2 cells during the repair process across all forms of injury (Suppl. Fig. 7f).
470

471 **Discussion**

472 These results show that AT2 fate plasticity exists in a time-window from late embryonic to early
473 postnatal life consistent in time with nascency. The timing and length of this window is dictated
474 by a molecular circuit driven by PRC2 and C/EBPα that together generate a pulse of *Dlk1,* a
475 known regulator of adult AT2 fate plasticity. Downregulation of C/EBPα occurs following injury
476 in the adult lung, is required to regenerate AT1 cells, and is mediated in part by the dominant
477 negative C/EBP family member CHOP. C/EBPα also suppresses an AT2 defensive state that is
478 mutually exclusive from fate plasticity that appears to be driven by interferon signaling.

479 From characterizing its nascent state, we determined AT2 cells first emerge around e15.5
480 at intermediate regions between the tips and stalks of the distal branches. Our findings
481 consolidate differing models on AT2 emergence, with our observed timing supporting the
482 bipotent model[4, 9, 10, 33, 37] and our observed pattern suggesting an intermediate starting point,
483 distinct from that proposed in both the bipotent (more proximal) and earlier differentiation[12]
484 (distal tip) models. After initial emergence (e15.5-16.5), subsequent AT2s next arise at proximal
485 regions coinciding with ASM-to-myofibroblast differentiation as previously reported[34]. Taken
486 together, these findings suggest more than one cue may be present to suppress alveolar epithelial
487 differentiation, one distal and another proximal in position. While it has been established that
488 distal tips are enriched in Wnt activity and thus retain stemness[74], it is unclear how more
489 proximally positioned DPs are suppressed. One compelling possibility is that ASM directly
490 suppresses differentiation of these proximally localized distal progenitors through direct
491 interaction on the basal epithelial surface, although it is unclear how said suppression is
492 molecularly mediated.

493 Our findings on AT2 emergence have also provided insight into the sequence of their
494 morphological changes. Given that basal extrusion occurs after AT2 molecular specification, it is
495 likely downstream of fate selection rather than an upstream regulator as previously proposed[75].
496 This observation is supported by prior work wherein AT2 fate selection was found to occur
497 under culture conditions that block basal extrusion[10]. If a byproduct of fate selection, what
498 purpose does basal extrusion serve? Following extrusion, we observe that some extruded AT2
499 cells engage with nearby epithelium from anatomically distinct branches, forming what we name
500 interlumenal junctions, or ILJs. We hypothesize basal extrusions are required to form these
501 junctions, that they are mediated in part by contraction of the AT2 lumenal surface, and likely

502 play a critical early role in postnatal alveologenesis, the stitching together of alveolar lumens[76].
503 While this process has been observed at the tissue level[14], as has the multilumenal nature of
504 mature AT2s[34], many questions remain as to the underlying cellular and molecular mechanisms
505 governing it. Further work on interlumenal junctions will be critical to understanding this stage
506 of alveolar maturation and assessing whether its disruption could underly diseases such as BPD
507 and COPD.

508 Following their emergence, nascent AT2 cells undergo transition towards their mature
509 AT2 transcriptional state over the course of ~7 days. This process occurs in a sporadic, salt and
510 pepper pattern distinct from the reported proximal-to-distal wave of alveolar epithelial fate
511 selection[13, 77] suggesting the cues driving maturation might arise from a different source, which is
512 likely to be immune given the genes enriched in mAT2s as well as prior studies demonstrating
513 interactions underlying one another's maturation[33] and function[15]. While AT2s have been shown
514 to impact macrophage maturation[33], an immune cell type has not been implicated in driving AT2
515 maturation during postnatal development. More work is needed to better understand which
516 immune cell types interact with AT2 cells during this process and determine how they impact
517 differentiation. While AT2 cells from both nascent and mature states retained plasticity, mAT2s
518 quickly lose this capability within the first week or so after birth, suggesting fate plasticity is
519 somewhat negatively correlated to AT2 maturation. Given these findings, we revised our model
520 of alveolar epithelial differentiation to include a fate plasticity window extending from e15.5
521 distal progenitors into AT2 nascency, and that tapers down over 1-2 weeks after birth. It is likely
522 this window is critical for postnatal alveologenesis and might be involved in the observed age-
523 dependent severity of COVID19[78].

524 While our bioinformatic screening for transcriptional regulators of the plasticity window
525 identified C/EBPα as a possible repressor, previous genetic deletions studies concluded that
526 *Cebpa* is required earlier for both AT1 and AT2 differentiation[46, 47]. As these findings conflict
527 with the observed expression pattern of C/EBPα, which is upregulated following AT2 fate
528 selection, we conducted sparse *Cebpa* deletion experiments in both DP and AT2 populations.
529 From these studies we found that *Cebpa* is dispensable for the selection but required for the
530 maintenance of AT2 fate, with the later finding recently confirmed in a manuscript by another
531 group[52]. The discrepancy is likely the result of the field's prior use of genetic tools now found to
532 cause toxicity in the developing mouse lung[48]. While our subsequent scRNAseq and ATACseq
533 analysis reveals repressive targets of C/EBPα, its positive transcriptional regulation of gene
534 expression has been demonstrated including recent publications [52]. While *Cebpa* loss does result
535 in a reduced expression of several AT2 mature genes, identified in both studies, it is important to
536 note that these AT2 cells do not concomitantly increase the expression of AT1 genes nor directly
537 convert into AT1 cells. Rather the AT2 program reverts to the nascent AT2 state, again
538 suggesting a repressive mechanism is at play that targets fate plasticity. While Sox9 was reported
539 in the other study to be upregulated following *Cebpa* loss, we only detected a modest increase at
540 the RNA level and screening of scRNAseq data referencing a DP gene list revealed no strong
541 upregulation, supporting our model that loss resulted in reversion to a more nAT2 state rather
542 than full dedifferentiation back to DP. Recent work has found that AT1s in the perinatal period
543 also retain fate plasticity and when stretch and YAP/TAZ signaling is lost they are capable to
544 AT1-to-AT2 differentiation[79]. While more work is needed to integrate those findings with ours
545 and others[52], one compelling model is that both perinatal AT2 and AT1 cells retain fate plasticity

546 for a period of time but are each suppressed by distinct repressors – C/EBPα for AT2s and
547 YAP/TAZ for AT1s.

548 Our investigation into the key gene(s) repressed by C/EBPα that could regulate fate
549 plasticity identified *Dlk1*, which encodes a cis-regulator of Notch signaling previously implicated
550 in AT2-to-AT1 conversion[23]. Notch is distinct from other signaling pathways in its use of cis-
551 regulators (like DLK1) for activation and has been shown to be critical in generating its well
552 characterized "salt and pepper" pattern[80]. While regulation of the *Dlk1* locus is well documented
553 to be mediated by an intergenic differentially methylation region (IG-DMR) downstream of the
554 gene[56, 81], ATAC-seq revealed no change in its accessibility nor any changes immediately
555 upstream of the gene's transcriptional start site upon loss of *Cebpa*. Rather, a dramatic change in
556 accessibility was observed in a previously uncharacterized region roughly 2 kilobases
557 downstream of the IG-DMR that the UCSC genome browser predicts is an enhancer. More work
558 is needed to determine how this element is regulated during development as well as repair
559 following injury in the adult lung.

560 Our investigation into developmental regulation of *Dlk1* expression determined that
561 PRC2 and C/EBPα act as a type 2 incoherent feedback loop to generate of pulse of DLK1
562 following downregulation of the PRC2 complex and likely its repressive epigenetic mark,
563 H3K27me3. While several feedback loops have been postulated and constructed in the field of
564 systems biology[62], most of the loops observed in eukaryotic cells are either type 1 coherent or
565 incoherent in configuration[62]. While the identified loop type (I2-FFL) is observed less frequently,
566 we believe the PRC2-C/EBPα regulation plays a critical role in timing and pattern of alveolar
567 epithelial differentiation, and future studies are needed to test whether reactivation of said loop
568 could be used to re-access AT2 fate plasticity in diseased lungs. We believe this feedback loop

569 constitutes a novel molecular circuit – a "pulse generator" of Notch activation, resulting in
570 spatial patterning of AT1 and AT2 differentiation through lateral inhibition. It is also conceivable
571 that disruption of this molecular circuit could result in an aberrant AT2 state that is disease
572 associated, such as those observed in models of IPF[82, 83].

573 Finally, our investigation into the adult lung demonstrates that C/EBPα downregulation
574 following injury is required for repair and is partly mediated by a C/EBP family member with
575 dominant negative activity, CHOP[70]. As CHOP is upregulated from various types of injury that
576 cause ER stress[84], it is still unclear how C/EBPα downregulation is stimulated following injury
577 of alveolar epithelial cell death, especially as we observe little to no C/EBPα downregulation
578 upon sparse AT2 ablation (Suppl. Fig. 7e). One compelling model requiring further inquiry is
579 that AT1 death sends a specific cue that downregulates C/EBPα to promote fate plasticity in
580 nearby AT2 cells and thus alveolar repair. Interestingly we found that *Cebpa* loss also allowed
581 AT2 cells to access what appears to be a pathogen defensive state driven by interferon signaling.
582 While presence of such a state is expected, as AT2 cells have been implicated in playing a role in
583 immune response in the lung[15], said state was not expected to be suppressed by C/EBPα nor to
584 be a mutually exclusive transcriptional state from the well-established regenerative DATP state[67,
585 85].

586 Taken together, these observations suggest that C/EBPα might suppress a larger program
587 that alternates between two states – one regenerative and the other defensive. If true, said
588 program would represent a more robust response to pathogen-mediated injury then previously
589 appreciated, as alternating between regenerative and defense states could ensure enough AT2s
590 are available at a given time to both promote clearance of the pathogen as well as repair damaged
591 alveoli (Fig. 7o).

592 We will briefly cover the limitations of this study to motivate and direct future work.
593 First, we dissociate murine lungs to form organoids which, while a common approach in the
594 field[10, 22, 34], might alter cellular phenotypes and promote fate plasticity. While the observed
595 behaviors of cultured DPs and AT2s largely match in vivo experiments[10, 22, 34] and velocity
596 analysis (Figure 3e-j), future work investigating fate plasticity more precisely in vivo would be
597 informative. Differences observed by normalized gene expression alone would benefit from
598 validation via ISH or immunostaining. As our study does not investigate whether AT1s derived
599 from DPs are distinct from those from AT2s, more work is needed to make said delineation. As
600 conclusions of scRNAseq cluster similarity can be impacted by cut-off points, more work
601 delineating differences in e15.5 DPs in an unbiased manner would be informative. While we
602 focused on the role of C/EBPα, future work on other genes from our screen would likely identify
603 other critical regulators of AT1/2 fate plasticity (see Suppl. Table 3). As BH3 death regulation is
604 studied only to determine its similarity between DPs, nAT2s, and mAT2s, more research is
605 needed to determine its role during development and repair. As CHOP expression was induced
606 using a smaller activator of PERK (CCT020312) that may stimulate off target molecules
607 conflating our experiments, further work is needed to precisely investigate the function of CHOP
608 in vivo. Finally, as our experiment revealing C/EBPα's regulation of a defensive AT2 state did
609 not directly introduce a pathogen, future work is needed to confirm said state is upregulated
610 following infection.
611

612 # Methods

613 ## Ethics

614 All mouse experiments followed applicable regulations and guidelines and were approved by the
615 Institutional Animal Care and Use Committee at the Mayo Clinic (Protocol# A00006319-21).
616 Mice were house under a 12 h light/12 h dark cycle and lights were not used during the dark
617 cycle. Mouse housing temperature was kept at 65-75 °F (~18-23 °C) and humidity at 40–60%.
618 Mice were housed in filtered cages and all experiments were performed in accordance with
619 approved Institutional Animal Care and Use Committee protocols and ethical considerations at
620 the Mayo Clinic.
621

622 **Mouse strains**

623 Timed-pregnant C57BL/6 J females (abbreviated B6; Jackson Laboratories) were used for all
624 embryonic time points, with gestational age verified by crown–rump length. For studies of adult
625 wild-type lungs, B6 males and females were used. Sparse labeling and recombination studies
626 were conducted by Cre recombinase expression using gene-targeted alleles BAC-*Nkx2.1*^{Cre},
627 LyzM (also called Lyz2)-Cre, and *Sftpc*$^{Cre\text{-}ERT2\text{-}rtTA}$[58]. Cre-dependent target genes were the
628 conditional "floxed" *Cebpa*[86] and *Ezh2*[87] for removal of *Cebpa* and *Ezh2* respectively. Two Cre
629 reporters were used: *Rosa26*^{mTmG} [88] (JAX stock #037456) and Tg(iSuRe-Cre) (MGI:6361145) [49].
630 Upon recombination, the Tg(iSuRe-Cre) allele labels the cell with membrane and cytoplasmic
631 tdTomato (tdT) and constitutively expresses Cre recombinase in the targeted cell, thus ensuring
632 that all Cre-conditional alleles are recombined, even under sparse or clonal conditions. For
633 initiating recombination with *Sftpc*$^{Cre\text{-}ERT2}$ (*Sftpc*^{CreER}), intraperitoneal injection of tamoxifen was
634 administered either at 20 mg/kg for complete (high dose) recombination in adult mice (> PN60),
635 or at 30 ng/kg for sparse recombination in perinatal mice (P0-P21), except where noted. EdU
636 (Cayman Chemicals 20518) was administered via drinking water at 0.1 mg/mL for the indicated

637 period of time. Genomic DNA was extracted from ear punches followed by Proteinase K (KAPA
638 Biosystems) digestion, and genotyping was performed by polymerase chain reaction (PCR) using
639 published primer sets.
640

641 ## Single-cell RNA-seq bioinformatic analysis

642 **Cell Isolation for library preparation**

643 Cells from PN25 *Sftpc*^{CreER}*; Tg(iSuRe-Cre);Cebpa*$^{wt/fl}$ and *Sftpc*^{CreER}*; Tg(iSuRe-Cre);Cebpa*$^{fl/fl}$
644 mice (2 weeks after TMX) were isolated and enriched (EpCAM^{+}) as per protocol described
645 below.
646

647 **scRNAseq library preparation and processing**

648 Single cell RNA sequencing was performed using the Chromium Single Cell 3' system (10x
649 Genomics) at the single cell sequencing core at Mayo Clinic according to manufacturer's
650 instruction (10x Genomics). Sequencing depth is an average of 75k reads per cell to detect lowly
651 expressed genes. Fastq files were generated using Cellranger v 7.2. The sequenced files were
652 mapped to the GRCm38/mm10, supplemented with tdTomato, PhiMut, and WPRE transcripts as
653 per the Tg(iSuRe-Cre) construct[49].
654

655 **scRNAseq data analysis**

656 We used Scanpy[89] and Seurat v.4.2.3[90] for processing and downstream analysis. In the Scanpy
657 pipeline, we identified highly variable genes using the scanpy function
658 scanpy.pp.highly_variable_genes with arguments min_mean = 0.0125, max_mean = 3, and
659 min_disp = 0.5. We restricted to this set of genes for downstream analysis. We further used

660 scanpy.pp.regress_out to regress out unwanted variation in the count of Unique Molecular
661 Identifiers (UMIs) and the percentage of mitochondrial reads. We ran scanpy's built in Principle
662 Component Analysis (PCA) algorithm with sc.tl.pca and default parameters. We then created a
663 nearest neighbor graph using sc.pp.neighbors with 200 neighbors and 50 Principle Components.
664 We then produced a UMAP dimensionality reduction with scanpy.tl.umap using min_dist =
665 0.001. We identified cell clusters through unsupervised clustering using the Leiden clustering
666 algorithm through with resolution = 0.8. We assigned cell labels to the clusters based on marker
667 gene expression, and removed several contaminating mesenchymal clusters. These clusters were
668 then visualized on the UMAP.

669 In the Seurat pipeline, doublets were estimated and removed using the DoubletFinder
670 Package[91]. Dead cells or outliers were excluded by removing cells with less than 500 features
671 and with more than 10% mitochondria gene content. Post alignment, the Seurat objects were
672 merged, normalized with LogNormalize method, and scaled. Top 3000 variable genes were used
673 to anchor. After PCA dimensional reduction with 30 principal components, we mapped our data
674 on UMAP projection with Louvain clustering algorithm. Subsequently canonical marker genes
675 for AT1 and AT2 cells[92] and sample conditions were used to assign cellular groups.

676 For RNA velocity, velocyto was used with default run command and run10x sub-
677 command to obtain velocity read counts[93]. For velocity analysis, we used Scanpy and scVelo
678 packages. The datasets were filtered by expression of < 200 genes or > 3200 genes, and genes
679 were expressed in < 3 cells. The dataset was subsequently normalized and the top 3000 highly
680 variable genes with a minimum 20 expressed count threshold were used in preprocessing. A
681 dynamical model was used to recover velocity estimate following Scvelo default parameters

682 (pp.moments(n_neighbors = 30), tl.recover_dynamics(fit_scaling = False), tl.velocity(mode =
683 'dynamical')).

684 We then produced velocity stream overlay on UMAP projection and latent time. We used
685 kmeans clustering from the SKlearn package to identify the two predominant directions of
686 velocity vectors within the nAT2 cell cluster. We then calculated an AT1/AT2 score in these
687 clusters based on expression of cell markers. We further performed partition-based graph
688 abstraction (PAGA)[94] based on the velocity vectors of each cell type to determine broader cell
689 type linkages[95].

690 For STITCH analysis (to generate SPRING plots), we ported in formatted datasets and
691 followed steps of logNormalization, and determined highly variable genes as instructed in the
692 Wagner 2018[96] example in MATLAB 2023a. The visualization was done using ForcedAtlas
693 layout in Gephi v7.2.1.

694 For analysis of lung development through embryonic, perinatal, and adult timepoints in
695 published scRNAseq datasets, the processed mRNA counts for each cell were used from
696 developing mouse lung datasets, (GSE119228)[33], (GSE113320)[12], and (GSE149563)[37]. Analysis
697 of bleomycin-induced lung injury on AT2 cells was performed on a published scRNAseq dataset
698 (GSE141259)[20].

699

700 Lung isolation and processing

701 For prenatal time points, individual embryos were staged by fetal crown–rump length before
702 sacrifice and lungs removed *en bloc*. For postnatal time points, mice were euthanized by either
703 carbon dioxide inhalation or intraperitoneal injection of Pentobarbital (Fatal-Plus Solution) and
704 dissected to both expose the lungs and allow for exsanguination via the abdominal aorta. 5-10

705 mL of phosphate buffered saline (PBS; Ca^{2+} and Mg^{2+} free, pH 7.4) was gently perfused into the
706 right ventricle of the heart by syringe with a 25-gauge needle until the lungs appeared white. For
707 postnatal time points (≥ 8 days), the trachea was then cannulated with either a blunt 22- or 25-
708 guage catheter, and the lungs were gently inflated to full capacity with molten low melting point
709 agarose (Sigma, 2% in PBS). For all time points, lungs were then separated by lobe and fixed in
710 4% PFA at 4 °C for either 1 h (e15.5 – e16.5), 1.5 h (e17.5), 2 h (e18.5 – PN10), or 4 h (>
711 PN10). For sectioning, a vibrating microtome (Leica) was used to generate embryonic (150 µm)
712 or adult (250 µm) tissue sections of uniform thickness.
713

714 **Immunostaining**

715 Immunohistochemistry was performed as previously described in Treutlein et. al.[9] using primary
716 antibodies against the following epitopes (used at 1:500 dilution unless otherwise noted): proSPC
717 (rabbit, Sigma AB3786), RAGE (rat, R&D MAB1179), E-cadherin (rat, Life Technologies
718 ECCD-2), PDPN (hamster, DSHB 8.1.1), MUC1 ((hamster, Thermo Scientific HM1630 and
719 rabbit (GeneTex GTX100459)), Alpha-SMA (1:100, mouse IgG2a, Invitrogen 50-9760-82),
720 EZH2 (ENX-1; mouse IgG2b, Santa Cruz Biotechnology sc-166609), KI67 (rat, Thermo
721 Scientific 14-5698-82), RELMα (rabbit, PeproTech 500-P214), CD74 (rat, BD Biosciences
722 555317), DLK1 (rabbit, R&D Systems MAB8634), C/EBPα (rabbit, Cell Signaling 8178),
723 LAMP1 (rat, DSHB 1D4B-s), and HOPX (rabbit, Abcam ab307671). Briefly, fixed lung slices
724 were permeabilized and blocked overnight in blocking buffer (5% goat serum/PBS/0.5% Triton
725 X-100) at 4 °C. Primary antibody incubation steps were conducted in blocking buffer over 3
726 nights and washing steps were performed in five rounds (30, 30 60, 90, and 90 min respectively)
727 using the blocking buffer. Primary antibodies were subsequently detected using Alexa Fluor-

728 conjugated secondary antibodies used at 1:1000 dilution unless otherwise noted, including Goat
729 anti-rabbit IgG Alexa 555 conjugated (Invitrogen, A21428), Goat anti-rabbit IgG Alexa 647
730 conjugated (Invitrogen, A32733), Goat anti-rat IgG Alexa 488 conjugated (Invitrogen, A11006),
731 Goat anti-rat IgG Alexa 647 conjugated (Invitrogen, A21247), Goat anti-hamster Alexa 647
732 (Invitrogen, A21451), and Goat anti-hamster Alexa 594 (Invitrogen, A21113) unless noted
733 otherwise. Secondary antibody incubation steps were conducted in blocking buffer over 2 nights
734 and washing steps were performed in five rounds (30, 30 60, 90, and 90 min respectively) using
735 PBT (0.1% Tween-20/PBS). For co-staining using antibodies from the same rabbit origins, we
736 performed sequential staining with 1-day anti-rabbit blocking between processes. In brief, we
737 stain with primary and secondary antibodies of the 1st marker as described, and then we block the
738 stained tissue with 40 µg/mL Fab Fragment Goat Anti-Rabbit IgG (Jackson ImmunoResearch,
739 AffiniPure™, 111-007-008) prior to the 2nd marker staining. EdU was detected using the standard
740 Click-iT reaction (Thermo Fisher). Lung slices were then mounted in Vectashield Mounting
741 Medium (Vector labs, H1000) and sealed with a coverslip. Images were acquired using a laser-
742 scanning confocal microscope (Zeiss LSM 780 and Leica Stellaris 8) and subsequently processed
743 using ImageJ.
744

745 **Timelapse Imaging**

746 Fluorescently lineage labeled mouse lung were sectioned at 200 µm thick using compresstome.
747 When imaging, we image sectioned slices in serum-free DMEM media on top of Matrigel for
748 stability, using Timelapse setup in LAS-X software for 24 h consecutively.
749

750 **Confocal Images 3D reconstruction**

751 We reconstructed 3D representation of cell imaging using IMARIS 10.2.1. The z-stack images
752 are imported as .tif images and reconstructed into 3D representation of tissue images. Marker
753 intensities are individually normalized thresholds for intensity and contrast, smoothing cellular
754 structures for interpretation accuracy, and removal background noise.
755

756 Cell isolation and culture

757 For time points e15.5, e18.5, and PN3, lungs were isolated *en bloc* without perfusion and pooled
758 by litter (6-8 lungs) for further processing. The lungs were then dissociated in 50 U/mL Dispase
759 (Corning 354235) and triturated with flame sterilized glass Pasteur pipettes of decreasing
760 diameters (1,000 µm, 800 µm, and 600 µm) to achieve a single-cell suspension. For PN25 and
761 adult time points, the lung was perfused with DPBS (Ca^{2+} and Mg^{2+} free, pH 7.4) as described
762 above. The trachea was punctured and then cannulated with a blunt 22-guage catheter, and the
763 lungs were inflated to full capacity with Dispase (~1 mL), and the trachea was sealed using a
764 non-absorbable silk suture. The inflated lobes were incubated in Dispase for 45 min at 25 °C on
765 a shaker.

766 For all time points, digested lungs were minced with a razor blade, suspended in 7 mL of
767 digestion buffer (RPMI-1640 containing FBS (10%, Corning), penicillin-streptomycin (1 U/mL,
768 Thermo Scientific), and DNase I (0.33 U/mL, Roche)), incubated at 4 °C for 10 min on a flat
769 shaker and triturated briefly with a 5-mL pipette.

770 To deplete red blood cells, an equal volume of AT2 isolation media (RPMI-1640
771 supplemented with penicillin-streptomycin (1 U/mL, Thermo Scientific), and DNase I (0.33
772 U/mL, Roche)) was added to the lung single-cell suspension. The suspension was passed through
773 a 100 µm mesh filter to remove residual tissue fragments and centrifuged at 400×g, 4 °C for 10

774 min. Pelleted cells were resuspended in 5 mL of red blood lysis buffer (BD Biosciences),
775 incubated for 2 min at room temperature, and neutralized with an equal volume of AT2 isolation
776 media. The suspension was passed through a 40 µm mesh filter (Fisher), centrifuged at 400×g, 4
777 °C for 10 min, and then resuspended in MACS buffer (2 mM EDTA, 0.5% BSA in PBS, filtered
778 and degassed) for purification.

779 The resultant single-cell suspension was incubated with Mouse Fc Blocking Reagent
780 (Miltenyi Biotec, 130-092-575) for 5 min at 4 °C. Other cell types were first depleted with
781 antibodies against CD45 (eBioscience, 13-0451-85), CD31 (BD Biosciences, 557355), Ter119
782 (eBioscience, 13-5921-85), CD140a (Miltenyi Biotec, 130-101-905), and CD104 (Miltenyi
783 Biotec, 130-106-922), followed by anti-biotin (Miltenyi Biotec, 130-090-485) magnetic
784 MicroBeads. Cell suspensions were passed through a 35 µm cell strainer (BD Biosciences) prior
785 to being loaded on LD columns (Miltenyi Biotec) as per the vendor's protocol. The flow through
786 was centrifuged at 300×g, 4 °C for 5 min and the pelleted cells were resuspended in MACS
787 buffer.

788 For positive selection of cell types, the following antibodies were used: anti-EpCAM
789 (clone G8.8, eBioscience, 13-5791-82) for e15.5 distal bipotent progenitors, anti-RELMα
790 (PeproTech, 500-P214BT) for e18.5 nascent AT2 cells, and either anti-CD74 or anti-MHC-II
791 (clone M5/114.15.2, eBioscience, 13-5321-82) for mature AT2 cells. Following antibody
792 incubation, the cells were then incubated with either anti-biotin or anti-rat IgG MicroBeads and
793 loaded on MS columns (Miltenyi Biotec) as per the vendor's protocol. The flow-through was
794 discarded and the column was taken off the magnet. The cells remaining in the column were
795 eluted with MACS buffer, resulting in a highly enriched preparation of either bipotent

796 progenitors (EpCAM$^+$), nascent AT2s (RELMα$^+$), or mature AT2s (MHC-II$^+$), unless noted
797 otherwise.

798 For culturing bipotent progenitors, nAT2s, or mAT2s, cell density and viability were
799 calculated using a Vi-CELL XR Cell Viability Analyzer (Beckman Coulter). Cells were cultured
800 in eight-well #1.5 coverglass chambers (Cellvis, C8-1.5H-N), pre-coated with growth factor
801 reduced Matrigel (85 µL, Corning 354230) for 30 min at 37 °C. The cells were plated at varying
802 densities: 30,000 cells/well (for e15.5 and e18.5), 60,000 cells/well for PN3), and 80,000
803 cells/well (for PN25 and adult). Cells were supplemented with FGF7 (50 ng/mL, R&D Systems
804 5028-KG-025), GSK126 (10 µM, ApexBio A3446), KL001 (12 µM, MedChemExpress HY-
805 108468), and interferon-γ (20 ng/mL, PeproTech 315-05) to the indicated concentrations in 400
806 µL of DMEM/F12 supplemented with penicillin-streptomycin (1 U/mL, Thermo Scientific).
807 Excluding FGF7, all other small molecules listed above were added after a 12h incubation period
808 to allow for cells to seed and adhere to the layer of Matrigel. Cells were maintained in an
809 incubator at 37 °C with 5% CO2/air, with media changes every other day typically for 4 days,
810 except where indicated otherwise.

811

812 **Flow cytometry**

813 We perform flow cytometry of AT2 cells using Miltenyl's Tyto flow sorter. Filtered and
814 RBC depleted lung cell isolates are to be incubated with 20 µL of each of the following 1:50
815 diluted primary antibodies: anti-RELMα, anti-CD74, and anti-MHC-II for 30 min at 4 °C. Cells
816 are washed with sorting buffer (Miltenyi, 130-107-207) and subsequently incubated with 20 µL
817 of each of the following secondary antibodies: (Anti-rabbit Alexa Fluor 647, anti-rat Alexa Fluor
818 405) for 30 min at 4 °C. Subsequently the sample are washed, filtered, and resuspended in 1 mL

819 sorting buffer and transfer to the sorting compartment of the cartridge (Miltenyi, 130-104-791).
820 Gates for markers positivity are drawn using unstained cells as negative controls.
821

822 **BH3 analysis**

823 Lung samples from mice of different ages (e15.5, e18.5, and ≥ PN60) were dissociated into a
824 single-cell suspension and enriched using relevant markers as described above. Cells were
825 stained on ice for 25 min away from light, then centrifuged at 200×g for 5 min, and subjected to
826 flow cytometry–based BH3 profiling as previously described by the Sarosiek lab[78]. Briefly, cells
827 were treated with activator or sensitizer BH3 peptides (New England Peptide) for 60 min at 28
828 °C in mannitol experimental buffer (MEB) [10 mM Hepes (pH 7.5), 150 mM mannitol, 50 mM
829 KCl, 0.02 mM EGTA, 0.02 mM EDTA, 0.1% BSA, and 5 mM succinate] with 0.001% digitonin.
830 Peptide sequences are as follows: BIM (Ac-MRPEIWIAQELRRIGDEFNA-NH2), BID (Ac-
831 EDIIRNIARHLAQVGDSMDRY-NH2), PUMA (p53 upregulated modulator of apoptosis) (Ac-
832 EQWAREIGAQLRRMADDLNA-NH2), BAD (Ac-LWAAQRYGRELRRMSDEFEGSFKGL-
833 NH2), Hrk (Harakiri) (Ac-WSSAAQLTAARLKALGDELHQ-NH2), and MS1 (MCL-1
834 specific) (Ac-RPEIWMTQGLRRLGDEINAYYAR-NH2). After peptide exposure, cells were
835 fixed in 2% PFA for 15 min which was then neutralized by addition of N2 buffer [1.7 M tris base
836 and 1.25 M glycine (pH 9.1)]. Cells were stained overnight with DAPI (1:1000, Abcam) and
837 anti–cytochrome c–Alexa Fluor 647 (1:2000, clone 6H2.B4, BioLegend) in a saponin-based
838 buffer (final concentration, 0.1% saponin; 1% BSA) and then analyzed by flow cytometry.
839 Cytochrome c release in response to BIM treatment was measured on an Attune NxT flow
840 cytometer (Thermo Fisher Scientific).
841

842 **Conditional deletion of *Cebpa* and *Ezh2 in vivo***

843 For conditional and efficient recombination of floxed alleles (*Cebpa*^{flox} or *Ezh2*^{flox}) at different
844 time points and cell types, we bred the floxed allele into one of four mouse lines, each with a
845 distinct combination of Cre and reporter alleles. For in vivo sparse cell labeling with efficient
846 recombination of either *Cebpa*^{flox} or *Ezh2*^{flo} alleles in distal progenitors, the *Tg*$^{Nkx2.1\text{-}Cre}$;
847 *Rosa26*$^{mTmG/mTmG}$ mouse line was used as we have previously found it sparsely labels DPs with
848 efficient flox allele recombination[10]. For sparse labeling of nAT2s with efficient recombination
849 of *Cebpa*^{flox}, the *LyzM*^{Cre}; *Rosa26*$^{mTmG/mTmG}$ mouse line was used as previously described[10]. For
850 broad labeling of AT2 cells with efficient *Cebpa*^{flox} recombination following a high dose of
851 tamoxifen (20 mg/kg), the *Sftpc*$^{Cre\text{-}ERT2}$; *Rosa26*$^{mTmG/mTmG}$ mouse line was used. Finally, to
852 sparsely label AT2s and retain efficient *Cebpa*^{flox} recombination following a low dose of
853 tamoxifen (30 ng/kg), the *Sftpc*$^{Cre\text{-}ERT}$; *Tg(iSuRe-Cre)* mouse line was used. Upon its
854 recombination, the *Tg(iSuRe-Cre)* allele constitutively expresses both the fluorescent lineage
855 label tdTomato as well as Cre recombinase, an approach that has been well established to
856 efficiently recombine multiple floxed under lower tamoxifen doses for targeting sparse cells[49].
857 To determine proliferation of AT2 cells, EdU (1 mg/mL) was administered in the drinking water
858 for the indicated period of time.

859

860 **ATAC-seq and CHIP-seq analysis**

861 Cells from PN25 *Sftpc*^{CreER}*; Tg(iSuRe-Cre); Cebpa*$^{wt/fl}$ and *Sftpc*^{CreER}*; Tg(iSuRe-Cre); Cebpa*$^{fl/fl}$
862 mice (2 weeks after TMX) were isolated and enriched (EpCAM^{+}) as per protocol described
863 above. Raw sequencing reads were trimmed of sequencing adapters and bad quality bases with
864 cutadapt version 2.8 in Trim Galore version 0.6.6 using default parameters. Bowtie2 version

865 2.5.0 (parameters: --end-to-end --very-sensitive --no-mixed --no-discordant --phred33 -I 10 -X
866 700) was used to map trimmed reads to the reference genome Mus_musculus.GRCm38. Picard
867 MarkDuplicates (v.2.26.10; http://broadinstitute.github.io/picard) was used for duplicate
868 removal. Reads were shifted by + 4 bp for those mapping to the positive strand and - 5 bp for
869 those mapping to the negative strand. ATAC-seq analysis was performed with HOMER(v 4.11).
870 Tag directories were made for each ATAC-seq run using HOMER[97] "makeTagDirectory". Peaks
871 for individual replicates were identified using the "findPeaks" command. To generate high-
872 confidence peak lists across both replicate samples for downstream analysis, ATAC-seq peaks
873 were identified using the HOMER "getDifferentialPeaksReplicates.pl" command. This command
874 uses DESeq2[98, 99] and identifies peaks that pass 2-fold enrichment and false discovery rate (FDR)
875 < 0.05 cutoffs. For these analyses, peak lists combining all peaks from the comparison conditions
876 were assembled. One condition was used as the target, and the other was used as background. To
877 characterize enriched motifs near differentially enriched peaks, we used HOMER's
878 "findMotifsGenome.pl" command to scan the entire peak by using "-size given" with standard
879 background. ATAC-seq peak annotation was performed using the homer annotatePeaks.pl
880 function to assign the nearest gene name to the peaks. To estimate the enrichment of
881 transcription factors and epigenetic modifications on the murine genome, we used the Cistrome
882 DB Toolkit analysis browser[61, 100] using default settings.
883

884 **Incoherent feed forward loop type 2 model fitting**

885 To assess whether the temporal expression pattern of *Dlk1* fit that predicted by a feed forward
886 loop we used the publicly available biocircuits package (https://biocircuits.github.io/) to
887 numerically solve the differential equations for a type 2, incoherent feed forward loop following

888 a step reduction of PRC2. After solving for a function over time for *Dlk1*, an R script was
889 generated to align its peak value to that observed in the scRNAseq timecourse and calculate a
890 goodness of fit by root mean squared error (RMSE). Parameters of the I2-FFL model were
891 independently varied until a good fit was reached (beta = 1.9, gamma = 5.5, and kappa = 3).
892

893 Mouse lung injury experiments and viral transfections

894 Lung injury was induced in adult mice by single-dose administration of bleomycin sulfate
895 (0.25mg/kg; VWR J60727-MA), which was dissolved in sterile saline and administered via
896 intratracheal (i.t.) administration. Lungs were isolated 16 days post injury and processed for
897 immunostaining.
898 To test whether C/EBPα is required for proper injury repair, adult *Rosa26*$^{mTmG/mTmG}$ mice were
899 administered either an AAV-*Sftpc-Cre* (control), or an AAV-*Sftpc-Cebpa-T2A-Cre* (prepared by
900 the Boston Children's Hospital Viral Vector Core (1.5×10^{14} GC (genome copies)/mL, serotype
901 2/9) and intratracheally instilled (5 µL of viral solution diluted in 45 µL PBS)) to overdrive
902 *Cebpa* expression and induce GFP labeling of AT2 lineage. A minimal 320 bp *Sftpc* promoter
903 element was used for both AAV preps. 5 days later, all mice were administered Fiin1
904 hydrochloride (14.75 mg/kg; Tocris 4002) via intratracheal instillation as described in out prior
905 work[10] or BHT (225 mg/kg; Sigma B1378) via intraperitoneal injection[71] to induce lung injury.
906 Lungs were isolated 14 days post injury and processed for immunostaining. For all intratracheal
907 instillation experiments, mice were anesthetized with isoflurane and kept in recovery under a
908 heat lamp.
909

910 Small molecule induction of CHOP

911 To induce CHOP expression in AT2 cells, *Sftpc*$^{CreERT2\text{-}rtTA}$; *Rosa26*$^{mTmG/mTmG}$ mice were first
912 administered tamoxifen (20 mg/kg) at PN11 for labeling of AT2 cells with GFP. 24 h later, mice
913 were either given corn oil (vehicle) or CCT020312 (MedChem Express HY-119240), a PERK
914 activator found to upregulate CHOP expression[101], at 2 mg/kg dissolved in corn oil via
915 intraperitoneal injection every 4 days (4 doses total). Lungs were isolated 2 weeks later and
916 processed for immunostaining.
917

918 Statistical analysis

919 Data analysis and all statistical tests were performed with GraphPad Prism software or R.
920 Replicate experiments were biological replicated using different animals, and the quantitative
921 values are presented as mean ± SD unless indicated otherwise. In graphs displayed as box plots,
922 the horizontal lines represent the median and error bars depict the $75^{th} - 25^{th}$ interquartile range
923 (IQR). Two-sided Student's *t*-tests (for normally distributed data), Mann-Whitney U-tests (for
924 data not normally distributed), and Brown-Forsythe and Welch ANOVA (for comparisons
925 between ≥ 3 groups) with Dunnett's multiple comparisons test were used to determine P-values.
926 No statistical method was used to predetermine sample size, and data distribution was tested for
927 normality prior to statistical analysis and plotting.
928

929 # Figure Legends

930

931 **Figure 1: Emergence and patterning of nascent AT2 cells.**

932 **a** scRNAseq data (GSE119228)[33] depicting embryonic, perinatal, and adult timepoints of
933 alveolar epithelial development. **b** Leiden Clustering analysis identifies four populations: mature
934 AT2s (mAT2), nascent AT2s (nAT2), distal progenitors (DP), and AT1s. **c** Stratification of the
935 AT2 lineage clusters across development depicting time separation of the DP, nAT2, and mAT2
936 cell populations. **d** Venn diagram showing number of genes detected for all clusters. **e** Dot plot
937 showing stage-restricted expression of selected surface markers for nAT2 and mAT2 cells,
938 *Retnla* and *Cd74* respectively. **f** e17.5 lung immunostained for nascent AT2 marker RELMα
939 (green), mature AT2 marker CD74 (red), and DP/AT1-restrictive luminal marker PDPN (white).
940 Bar, 25 µm. **g** e15.5 (left) and e16.5 (right) lungs immunostained for ASM cell marker smooth
941 muscle actin (SMA, red), RELMα (green), epithelial marker E-cadherin (ECAD, blue), and
942 PDPN (white). Close-up images for e15.5 lungs depict rare cases of single nAT2 cells (asterisk)
943 emerging in intermediate regions, but not at the terminal end buds (arrowheads). Bars, 100 µm
944 (left and right panels), 20 µm (close-ups). Mesothelium marked with white dash. **h**
945 Quantification of RELMα$^+$ nAT2 emergence in distal epithelial branches across development
946 from e15.5 to e17.5 determined by immunostaining (*n* represents branches scored for each
947 timepoint). ****$p \leq 0.0001$ (Brown-Forsythe and Welch ANOVA test). **i** Quantification of
948 RELMα$^+$ nAT2 anatomical positioning (columnar versus basally extruded) across development.
949 Extruded values presented as mean ± SD (*n* represents cells scored at each timepoint). **j**
950 Schematic showing region of AT2 Emergent Zone (green) within Sox9$^+$ distal epithelium at the
951 terminal stalk (blue) instead of Sox2$^+$ airway epithelium region. Around 17.5, nAT2 cell
952 (RELMα$^+$) basally extrude and then junction in distal epithelial branches and propagate emergent

953 zone proximally further. Near birth (PN0), as proximal regions further developed, emergent
954 zones shift to TEB.
955
956 **Figure 2:**
957 **a** e17.5 lung immunostained for RELMα (green), PDPN (white), and DAPI (blue). **a-i** depicts a
958 RELMα^{+} nAT2 cell traversing across the interstitium from lumen A to B. Close-up panels (right)
959 show a nAT2 cell embedded in lumen A, at z-position +18 µm (top right), as well as in lumen B,
960 at z-position +24 µm (bottom right). Bar, 50 µm (left), 10 µm (close-ups; right). **b** Quantification
961 of nAT2 interlumenal junctioning (ILJ) events detected during development by immunostaining
962 (*n* represents nAT2 cells scored at each timepoint). ****$p = 4.8 \times 10^{-11}$ (one-way ANOVA, data
963 as mean ± SD). **c** 3D rendering immunostaining of single (upper) and double (lower)
964 interlumenal junctioning nAT2s for E-cadherin (green), RELMα (red), PDPN (white), and DAPI.
965 Lumen boundaries are marked in yellow dashes. **d** experimental schematics of timeplase
966 confocal microscopy on *Nkx2.1*^{Cre}*; Rosa26*^{mTmG} lineage labeled precision cut lung slices at distal
967 lung. **e** Single nAT2 junctions between two lumens in 12-hour snapshots. **f** Two nAT2s
968 established contact at 14.5 hr and junction between two lumens in 15-hour snapshots, contact
969 marked with white arrows. **g** Examples of luminal Muc1 domain length in non-junctioning (left)
970 and junctioning nAT2s **h** Quantification of (g) shows condensed MUC1 domain in ILJ nAT2s**.** (*n*
971 represents number of nAT2 cells scored at each timepoint). ****$p = 4.8 \times 10^{-11}$ (Student's two-
972 sided *t*-test, data as mean ± SD). **i** schematics of stages of interluminal junctioning, including
973 nAT2 basal extrusion and apical domain constriction **j** schematics of nAT2 extrusion and
974 junctioning outcomes at various interstitial positions.
975

976 **Figure 3: Nascent AT2s retain fate plasticity.**

977 **a** PN1 and adult (≥ PN60) lungs immunostained for AT2 marker MUC1 (white), RELMα
978 (green), CD74 (red), and DAPI. Bar, 10 µm. **b** Timecourse quantification of (**a**) showing AT2
979 transitioning from nascent (RELMα$^+$) to mature (CD74$^+$). (*n* represents total AT2 cells scored at
980 each timepoint in experimental triplicate, values as mean ± SD). ****$p \leq 0.0001$ (one-way
981 ANOVA, data as mean ± SD). **c** PN1 lung immunostained for RELMα (green), CD74 (red), and
982 DAPI. Close-up showing both CD74$^+$ mAT2s and RELMα$^+$ nAT2s. Bar, 50 µm. **d** Alveolar fate
983 selection during late embryogenesis, contrasted with AT2 maturation during the early post-natal
984 period. **e** PAGA velocity of scRNAseq data of e15.5 and e17.5 epithelial cells. Arrow thickness
985 represents the relative fraction of cells with velocity from the original cluster to target cluster. A
986 transcriptional trajectory is observed starting from nAT2s to nAT1s (red arrow). **f** Velocity
987 magnitude and AT1/AT2 gene score for the nAT2 fraction from (**e**). **g** Velocity analysis of the
988 nAT2 fraction from (**e**) depicting AT1/AT2 score (cutoff 0.5). **h** scRNAseq data (GSE149563)[37]
989 of embryonic, perinatal, and adult time points of the distal epithelium. **i** Leiden clustering
990 including a distinct transitional AT2 cluster (tAT2 > 1; brown). Close-up depicts velocity
991 analysis (red dotted box), showing transition towards AT1 cluster. **j** Timepoint distribution of
992 cells observed within tAT2 > 1 cluster in (**i**). **k** Immunostained spheroids of e15.5 distal
993 progenitors (EpCAM$^+$), e18.5 nAT2s (RELMα$^+$), PN3 mAT2s (MHC-II$^+$), and adult mAT2s
994 (MHC-II$^+$). Spheroids were cultured on Matrigel for four days with media supplemented every
995 two days with FGF7 (50 ng/mL), followed by fixation and stained for PDPN (white), RAGE
996 (red), DAPI (blue), and AT2 marker SFTPC (green). Cells that remained distal progenitors
997 retained both AT1 markers (RAGE, PDPN) and the AT2 marker (SFTPC). Bars, 20 µm. **l**
998 Quantification of (**k**) showing percentage of cells per spheroid that differentiated into AT1 cells

999 determined by immunostaining (*n* = spheroids sampled for each condition in experimental
1000 triplicate). ****$p \leq 0.0001$ (one-way ANOVA). **m** A revised model of the Fate Plasticity
1001 Window depicting retained fate plasticity in nAT2 cells with the ability to differentiate into AT1
1002 cells. All experiments were repeated at least three times.
1003
1004 **Figure 4: C/EBPα a is required to maintain but not select AT2 fate.**
1005 **a** A bioinformatic screen of 1,678 transcription factors or epigenetic regulators, out of which 67
1006 are enriched along the AT2 lineage. A final list of 32 genes were selected that have known
1007 embryonic lethal or lung defects upon knockout in mice. These 32 genes stratify into four time-
1008 dependent categories: DP restrictive, DP-nAT2 restrictive, nAT2-mAT2 restrictive, and
1009 constitutive. The Plasticity Window (red dotted box) spans from ~e16.5 to ~PN7. **b** Dot plot
1010 showing expression of *Sox9* (DP restrictive; yellow), *Cebpa* and *Nupr1* (nAT2-mAT2 restrictive;
1011 pink), *Etv5* and *Elf5* (constitutive; grey) over developmental and adult timepoints. The plasticity
1012 window is depicted with a red dotted box. **c** e16.5 and e17.5lungs immunostained for PDPN
1013 (white), C/EBPα (green), E-cadherin (ECAD, red), and DAPI (blue). C/EBPα^{+} cells are marked
1014 (arrowheads) within the proximal (P) and distal (D) regions of the epithelial branches. Bars, 100
1015 µm. **d** Alveolar regions of PN0 control *Nkx2.1*^{Cre}*; Rosa26*^{mTmG}*; Cebpa*$^{wt/fl}$ (left) and *Nkx2.1*^{Cre}*;*
1016 *Rosa26*^{mTmG}*; Cebpa*$^{fl/fl}$ (right) lungs immunostained for Cre reporter (mTmG) and MUC1
1017 (white). GFP^{+} (DP lineage) cells form both AT1 cells (flattening; "1") and AT2 cells (MUC1^{+})
1018 even upon *Cebpa* deletion. Bars, 50 µm. **e** Alveolar regions of adult control *LyzM*^{Cre}*;*
1019 *Rosa26*^{mTmG}*; Cebpa*$^{wt/fl}$ (left) and *LyzM*^{Cre}*; Rosa26*^{mTmG}*; Cebpa*$^{fl/fl}$ (right) lungs immunostained
1020 for MUC1 (white) and CD74 (blue). AT2-lineage derived GFP^{+} cells are seen to differentiate
1021 into flat AT1 cells (asterisk) upon *Cebpa* deletion. Bars, 100 µm. **f** Quantification of (**e**) showing

1022 percent GFP$^+$ cells that differentiate into AT1s upon *Cebpa* deletion (*n* represents number of
1023 GFP$^+$ cells sampled for the *Cebpa*$^{wt/fl}$ and *Cebpa*$^{fl/fl}$ conditions in experimental triplicate). ****p
1024 $= 1.4 \times 10^{-14}$ (Student's two-sided *t*-test, data as mean ± SD). All experiments were repeated at
1025 least three times.
1026

1027 **Figure 5: C/EBPα blocks AT2 fate plasticity by repressing Dlk1.**

1028 **a** Experimental setup and timeline: Lungs were isolated 14 days post TMX (PN25) and alveolar
1029 epithelial cells (EpCAM$^+$) from control (*Sftpc*^{CreER}*; Tg(iSuRe-Cre); Cebpa*$^{wt/fl}$) and *Cebpa*
1030 deleted (*Sftpc*^{CreER}*; Tg(iSuRe-Cre); Cebpa*$^{fl/fl}$) lungs were processed for scRNAseq. **a-i** depicts
1031 the clusters (Louvain). **a-ii** shows gene scores across the 3 clusters in (**ai**). Upon *Cebpa* deletion,
1032 AT2 and mAT2 scores decreases, while nAT2 score increases compared to control AT2s without
1033 activation of AT1 score of the *Cebpa*$^{fl/fl}$ cluster (red dashed box). **b** Experimental timeline and
1034 TMX dosage. EdU water administered continuously for 14 days. Lungs immunostained for tdT
1035 (red) and proliferation (detected by ClickIT in green). *Cebpa* deleted lungs with either high
1036 (~99% AT2s) or sparse dose (~20% AT2s) TMX, depicting proliferating AT2-lineage cells
1037 (asterisk) and flattening AT1 cells (arrowhead). Bars, 50 µm. **c** Quantification of (**b**) showing
1038 percent tdT$^+$ AT1 cells upon *Cebpa* deletion in either High Dose (fl/fl – H.D.) or Sparse (fl/fl –
1039 Sp) deletions compared to control (wt/fl) AT2s (*n* represents tdT$^+$ cells sampled for each
1040 condition in experimental triplicate). ****$p \leq 0.0001$ (One-way ANOVA with Tukey's multiple
1041 comparisons testing; data as mean ± SD). **d** Average gene expression values ($\log_2$ fold change) of
1042 the 22 (out of 107 total) genes that encode for extracellular proteins enriched in the *Cebpa*$^{fl/fl}$
1043 AT2 cluster. Six genes (bold) are found to be upregulated in nAT2 cells and four of which
1044 encodes secreted (green) or membrane bound (red) protein, with *Dlk1* (red, bold) having the

1045 highest fold expression (log_2 fold change). **e** Alveolar regions of lungs from control *Sftpc*^{CreER};
1046 *Tg(iSuRe-Cre); Cebpa*$^{wt/fl}$ (left) or *Sftpc*^{CreER}; *Tg(iSuRe-Cre); Cebpa*$^{fl/fl}$ (right) mice, isolated 14
1047 days post high-dose TMX (at PN25). Lungs were immunostained for DLK1 (green) and tdT
1048 (red). Bars, 20 µm. **f** Quantification of (**e**) for percent TdT$^+$ AT2 cells that express DLK1 upon
1049 loss of *Cebpa* in both high dose and sparse deletion conditions. Note similar percentage of tdT$^+$
1050 AT2s express DLK1 in both high dose and sparse deletion conditions, 47.2% and 43.9%
1051 respectively (*n* represents tdT$^+$ cells sampled for control, high dose and sparse deletion in
1052 experimental triplicate). ****$p \leq 0.0001$, *$p = 0.015$ (one-way ANOVA, data as mean ± SD). All
1053 experiments were repeated at least three times. **g** Bulk ATACseq tracks showing chromatin
1054 accessibility of *Cebpa*$^{wt/fl}$ (blue) and *Cebpa*$^{fl/fl}$ (red) AT2 cells ($n = 3$ replicates for each
1055 condition), showing the *Dlk1* transcriptional start site (TSS) and the intergenic differentially
1056 methylated region (IG-DMR). The closest C/EBPα binding site to the *Dlk1* TSS is observed at a
1057 distal trans-regulatory element (TRE, yellow), downstream of the IG-DMR, with reduced
1058 chromatic accessibility upon loss of *Cebpa*. Further reanalysis of ChIP-seq dataset of the TRE
1059 (red dashed box) shows elevated activity at binding sites, indicating their involvement in *Dlk1*
1060 regulation.
1061

1062 **Figure 6: PRC2 and C/EBPα act as an incoherent FFL to generate a DLK1 pulse late in**
1063 **development.**

1064 **a** Distal alveolar buds of e15.5 (top) and e17.5 (bottom) lungs immunostained for DLK1 (green)
1065 and E-cadherin (ECAD, red). Close-up images show e15.5 tips have low DLK1 intensity (fire
1066 LUT), and e17.5 tips have higher levels of DLK1 protein. Bars, 10 µm. **b** Dot plot showing RNA
1067 expression levels of *Cebpa*, *Dlk1*, and PRC2 members genes (red) during developmental time-

1068 course. Minimal expression of *Cebpa* and *Dlk1* observed (grey dashed box), in contrast to the
1069 high PRC2 members genes before e16.5. **c** Epithelial branches of e16.5 and e17.5 lungs
1070 immunostained for PDPN (white), EZH2 (green), and E-cadherin (ECAD, red). EZH2 presence
1071 in the proximal (P) and distal (D) regions of the epithelial branches at e16.5 but absence by
1072 e17.5. Bars, 50 µm. **d** Immunostained spheroids of e15.5 DPs ($EpCAM^+$) cultured on Matrigel
1073 for four days with media supplemented every two days with FGF7 alone (Control, top) or FGF7
1074 with GSK126 (10 µM), an EZH2 inhibitor (bottom). Note an increase in DLK1 (red) in cultures
1075 with GSK126. Bars, 20 µm. **e** Quantification of (**d**) showing percent $DLK1^+$ cells per spheroid
1076 for each condition in the culture at day 4 determined by immunostaining (*n* represents number of
1077 spheroids for each condition in experimental triplicate). ****$p = 8.24 \times 10^{-15}$ (Student's two-
1078 sided *t*-test, data as mean ± SD). **f** Cistrome DB Toolkit analysis at the *Cebpa* locus identifies
1079 EZH2 (red) and the other PRC2 members (grey) to have enriched binding at this site. **g**
1080 Immunostained spheroids of e15.5 DPs cultured as in (**d**). Note an increase in C/EBPα (red) in
1081 GSK126 group. Bars, 20 µm. **h** Quantification of (**g**) for percent $C/EBP\alpha^+$ cells per spheroid at
1082 day 4 determined by immunostaining (*n* represents number of spheroids for each condition in
1083 experimental triplicate). ****$p = 3.9 \times 10^{-36}$ (Student's two-sided *t*-test, data as mean ± SD). **i**
1084 Distal epithelial branch of an e15.5 $Nkx2.1^{Cre}$; $Rosa26^{mTmG}$; $Ezh2^{fl/fl}$ mouse lung, sparsely
1085 labeling and deleting *Ezh2* in (GFP^+) alveolar epithelial cells. Lungs were immunostained for
1086 C/EBPα (white) and the Cre reporter (mTmG). Bar, 10 µm. **j** Quantification of (**i**) showing
1087 percent of DP cells in the distal alveolar buds expressing C/EBPα in lineage negative (RFP^+) or
1088 lineage positive (GFP^+) cells (*n* represents number of distal alveolar buds sampled for both
1089 groups). ****$p \leq 0.0001$ (Mann-Whitney U-test). **k** Interactions between EZH2/PRC2, C/EBPα,
1090 and DLK1 that fits the model of an incoherent, type 2 Feed Forward Loop (I2-FFL). **l** Model

1091 fitting of *Dlk1* expression from scRNAseq data of the developing lung[37], following the DP >
1092 nAT2 > mAT2 lineage fitted onto an I2-FFL Model (red line). RMSE = 0.12 (High goodness of
1093 fit if RMSE ≤ 0.75). **m** Spheroids of e15.5 DPs cultured as in (**d**), immunostained for PDPN
1094 (white), SFTPC (green), RAGE (red), and DAPI. Note that treatment with GSK126 increases the
1095 proportion of AT2 differentiation detected by an increase in $SFTPC^+$ (green) cells. Bars, 20 µm.
1096 **n** Quantification of (**m**) showing a stacked plot of the proportion of DP (white), AT1 (grey) and
1097 AT2 (black) cells determined by immunostaining. Compared to control, Both GSK126 alone and
1098 FGF7 + GSK126 groups resulted in significantly more AT2 differentiation (*n* represents number
1099 of spheroids for each condition in experimental triplicate). ****$p = 3.3 \times 10^{-43}$ for Control vs
1100 GSK126, $p = 2.0 \times 10^{-36}$ for Control vs FGF7 + GSK126 (one-way ANOVA, data as
1101 mean ± SD). **o** Schematic of DLK1 pulse upon removal of repressors reopens AT2 fate plasticity
1102 window and convert a subset of AT2s into Notch signaling senders. In conjunction of further
1103 lateral inhibition, the molecular circuit in (**k**) contributes to AT1/AT2 patterning in lung
1104 development. All experiments were repeated at least three times.
1105

1106 **Figure 7: C/EBPα downregulation is required to re-access mutually exclusive Defender and**
1107 **Regenerative states in response to injury.**
1108 **a** Experimental design (top). 5 days after AAV-SPC-Cre (Control; left) or AAV-SPC-Cebpa-
1109 T2A-Cre (right) instillation into lungs of adult *Rosa26*^{mTmG} mice to induce constitutive GFP-Cre
1110 expression and overdrive expression of *Cebpa* in AT2 cells, lungs were injured by Fiin1 (14.75
1111 mg/kg) intratracheal instillation (i.t.). Lungs were isolated and immunostained for Cre reporter
1112 (GFP) and AT1 markers 14 days post injury (dpi). Immunostained images (bottom) show GFP^+
1113 AT1 cells (asterisk) in the control, but little to none when C/EBPα is overexpressed. Bars, 100

1114 μm. **b** Quantification of (**a**) for percent GFP^+ cells that differentiated into AT1 cells (*n* represents
1115 GFP^+ cells sampled for each condition in experimental triplicate). ****$p = 6.5 \times 10^{-10}$ (Student's
1116 two-sided *t*-test, data as mean ± SD). **c** Alveolar regions of an adult mouse lung 16 days post 1X
1117 Bleomycin (0.25 mg/kg, i.t.) injury, immunostained for E-cadherin (ECAD, green), C/EBPα
1118 (red), and DAPI (blue). Injured (right) sites show simplified alveolar structures with reduced E-
1119 cadherin expression compared to uninjured sites (left). C/EBPα breakout (fire LUT) below
1120 depicts reduced C/EBPα expression in injured versus uninjured sites. Bars, 100 μm. **d**
1121 Quantification of (**c**) for mean C/EBPα intensity in AT2 cells within uninjured or injured regions
1122 (*n* represents cells scored for each condition in experimental triplicate). ****$p \leq 0.0001$ (Mann-
1123 Whitney U-test). **e** Dot plot from a scRNAseq dataset (GSE141259)[20] of 1X bleomycin-induced
1124 injury in AT2 cells, showing relative gene expression in vehicle (control) and various timepoints
1125 post 1X Bleomycin injury. Spikes in expression of DATP state associated genes (*Ddit3*, *Atf3*,
1126 *Atf4*, and *Ezh2*) are marked (dashed red box), whereas a temporary reduction of *Cebpa* is
1127 observed upon injury. The DATP gene score (red, see Suppl. Table 1) is also plotted on this
1128 timecourse, showing an activation of a DATP associated state upon injury, which resolves over
1129 time. **f** Experimental design for lineage labeling AT2 cells at PN11 in *Sftpc*^{CreER}; *Rosa26*^{mTmG}
1130 mice, followed by administration of corn oil (vehicle) or CCT020312 (2 mg/kg, intraperitoneal),
1131 a Ddit3 agonist, 1 day post TMX, and every 4 days (4 doses total). Lungs were isolated 14 days
1132 post TMX (PN25) and immunostained for Cre reported (mTmG) and MUC1 (white). Upon
1133 treatment with CCT020312, an increase in GFP^+ AT1 cells (asterisk) is observed. Bars, 50 μm. **g**
1134 Quantification of (**f**) showing percent GFP^+ AT1 cells for either vehicle or CCT020312
1135 conditions (*n* represents GFP^+ cells sampled for each condition). ****$p = 2.1 \times 10^{-11}$ (Student's
1136 two-sided *t*-test, data as mean ± SD). **h** Leiden clustering of our scRNAseq dataset reveals two

1137 distinct *Cebpa*$^{fl/fl}$ AT2 clusters: AT2^{DLK1+} (green) and AT2^{Def} (red). Velocity analysis (arrows)
1138 show AT2^{DLK1+} cells going in two separate trajectories, towards the AT1 and AT2^{Def} clusters. **i**
1139 Gene Ontology (GO) analysis of the AT2^{Def} cluster shows enriched pathogen defense response
1140 (red) and interferon signaling (black) gene programs. **j** DATP- and Defender-associated gene
1141 score co-expression shows a mutually exclusive pattern in *Cebpa*$^{fl/fl}$ cells. **k** SPRING plot of the
1142 four clusters observed in (**h**), showing AT2^{Def} state (red) in between the control AT2 (orange)
1143 and AT2^{DLK1+} (green) clusters. **l** SPRING plot of the DATP-associated gene score showing a
1144 high DATP score between the control AT2 (middle) and AT1 (left) clusters. **m** Immunostained
1145 spheroids of PN3 mAT2s cultured on Matrigel for four days with media supplemented every two
1146 days with FGF7 alone (Control, top) or with interferon-γ (20 ng/mL) (bottom). Note a decrease
1147 in AT1 cells (asterisk) in cultures treated with interferon-γ. Bars, 20 µm. **n** Quantification of (**m**)
1148 showing percent of cells per spheroid that differentiated into AT1s for each condition (*n*
1149 represents spheroids sampled per condition). ****$p = 1.2 \times 10^{-8}$ (Student's two-sided *t*-test, data
1150 as mean ± SD). **o** Schematic showing AT2 oscillation between AT2^{Def} (purple) and AT2^{DATP}
1151 (yellow) states, negatively regulated by C/EBPα. Upon AT2 loss (grey AT2s) due to infection,
1152 remaining AT2s can oscillate (left) between the two states resulting in proper infection response
1153 and regeneration. The inability to access either the AT2^{Def} or AT2^{DATP} states would result in
1154 impaired pathogen response or impaired repair and regeneration respectively. All experiments
1155 were repeated at least three times.
1156

1157 **Supplementary Figure 1: Dynamics of nascent AT2 state and emergence**

1158 **a** Cluster correlation analyzing the strength of correlation between each of the four clusters
1159 detected: AT1, DP, nAT2, and mAT2. Pearson Correlation > 0.5 indicates a strong, positive

1160 correlation. **b** Coassignment probability for the four clusters shown in (**a**), measuring the
1161 probability of merging two clusters. Note that the nAT2 and mAT2 clusters do not have a
1162 significant coassignment probability (asterisk), indicating they are distinct, stable cell
1163 populations. Low coassignment probability (< 0.5) represents a stable cluster with respect to one
1164 another. **c** scRNAseq expression for genes enriched for the clusters identified within the AT2
1165 lineage. *Cd74* and *Retnla* are highlighted (bold) as being surface markers chosen for mature and
1166 nascent AT2s respectively. **d** feature plot of *Retnla* and *Cd74* in mouse development timecourse
1167 dataset from Cohen et al., showing high and exclusive expression patterns of the nascent and
1168 mature AT2 cell markers. **e** e17.5 lung immunostained for PDPN (white), distal progenitor
1169 marker SOX9 (green), nAT2 marker RELMα (red), and DAPI (blue). Nascent AT2 cells are
1170 marked (arrowhead) to show them as RELMα^{+} and SOX9^{low}. **f** Quantification of nAT2 clustering
1171 observed as either singlets, doublets, or in clusters of ≥ 3 across embryonic timepoints from
1172 e15.5 to PN0 (*n* = 30 nAT2 clusters scored at e15.5, 155 at e16.5, 144 at e17.5, 228 at e18.5, 140
1173 at e19.5, and 96 at P0). **g** flow cytometry of EpCAM^{+} nascent AT2s from *WT embryonic* mouse
1174 lung, show moderate RELMα positivity, and low labeling efficiency by CD74, suggesting that
1175 nascent AT2s can be labeled and sort by RELMα. **h** flow cytometry of tdT^{+} mature AT2s from
1176 *Sftpc^{CreER}; Tg(iSuRe-Cre)*mouse lung, show little RELMα positivity, moderate labeling
1177 efficiency by CD74, and high labeling efficiency by MHC-II, suggesting that MHC-II is more
1178 effective as cell isolating marker comparing to CD74.
1179

1180 **Supplementary Figure 2: Spatial and Temporal Characterization of junctioning nAT2s**
1181 **a** Cross-section of e17.5, e18.5, or PN0 distal lungs slices immunostained for RELMα (red),
1182 DAPI (blue), and markers of interests (green), including C/EBPα, EZH2, DLK1, SFTPC,

1183 LAMP1, MUC1, PDPN, RAGE, and HOP. **b** Quantification of portion of nAT2 showing their
1184 high positivity in AT2 character and fate plasticity and their absence of AT1 character. **c**
1185 Additional 3D renderings on immunostaining of double interlumenal junctioning nAT2s for E-
1186 cadherin (ECAD) or RAGE (green), RELMα (red), PDPN or MUC1 (white), and DAPI (blue).
1187 Lumen boundaries are marked in yellow dashes. **d** Additional snapshots timeplase confocal
1188 microscopy on *Nkx2.1*^{Cre}; *Rosa26*^{mTmG} lineage labeled precision cut lung slices at distal lung
1189 showing dynamics interlumenal junctioning.
1190
1191 **Supplementary Figure 3: Details on state dependent plasticity and death sensitivity**
1192 **a** Cross-section of an airway (dashed yellow) of e17.5 (left) and PN1 (right) lungs
1193 immunostained for RELMα (green), CD74 (red) and DAPI (blue). Airway region at PN1 shows
1194 presence of RELMα in the airway epithelium, but the absence at e17.5 confirms its specificity to
1195 nAT2s during the AT2 fate selection window. Bars, 25 µm. **b** Proximal and distal epithelium of a
1196 PN1 lung immunostained for RELMα (green), CD74 (red) and DAPI (blue), showing salt-and-
1197 pepper pattern of AT2 maturation. Bar, 50 µm. **c** scRNAseq UMAP of distal lung epithelium at
1198 e15.5 (blue) and e17.5 (orange) timepoints. **d** Merged clusters of scRNAseq dataset in (**c**),
1199 showing three e15.5 distal epithelium (DE) clusters, and three e17.5 clusters (DP, nAT2, and
1200 nAT1). **e** Cluster correlation of the six clusters observed in (**d**). No significant correlation
1201 observed between either e15.5 DE cluster with the nAT2 or nAT1 clusters at e17.5. A weak
1202 correlation (0.42, dashed box) observed between the e15.5 DE3 and e17.5 DP clusters. **f**
1203 Pseudotime trajectory analysis showing e15.5 cells are the primary root cells of origin (left) and
1204 e17.5 AT1 cells are endpoint cells (right). **g** Velocity trajectories showing transition from e15.5
1205 DE clusters to e17.5 DP cells. Subsequent trajectories lead either directly to AT1 cells or

1206 indirectly, transitioning through the nAT2 cluster. **h** BH3 death sensitivity assay of e15.5 DP,
1207 e18.5 nAT2, and ≥ PN60 mAT2 cells, showing percent cytochrome c release upon treatment
1208 with activator or sensitizer BH3 peptides. A higher cytochrome c release percentage indicates
1209 increased sensitivity to BH3-mediated apoptosis. Alam and DFNA5 are positive controls; DMSO
1210 is the vehicle control and PUMA 2A is an inactive peptide negative control. Cytochrome c
1211 release (%) values are presented as mean ± SD. ****$p \leq 0.0001$, ***$p \leq 0.001$ (one-way
1212 ANOVA, comparing DP and mAT2 cells).
1213
1214 **Supplementary Figure 4: Bioinformatic screen for regulators of AT2 plasticity and**
1215 **perinatal *Cebpa* deletion.**
1216 **a** Heat map showing expression of all 32 genes from Figure 4a. Cells (columns) are arranged in
1217 developmental pseudotime (DP, nAT2, mAT2; left to right) along the AT2 lineage. Note that the
1218 "mAT2 (TM)" is from the Tabula Muris scRNAseq dataset (GSE109774)[41], which sequences
1219 AT2 cells more deeply. Genes form four patterns: constitutive (grey), DP restrictive (blue), DP-
1220 nAT2 restrictive (orange), and nAT2-mAT2 restrictive (pink). **b** Dot plot of the transcription
1221 factors from (**a**) that are expressed within the plasticity window (red dotted box), showing
1222 expression at different developmental and adult timepoints. **c** Alveolar regions of PN0 control
1223 *Nkx2.1*^{Cre}*; Rosa26*^{mTmG}*; Cebpa*$^{wt/fl}$ (left) and *Nkx2.1*^{Cre}*; Rosa26*^{mTmG}*; Cebpa*$^{fl/fl}$ (right) lungs
1224 immunostained for MUC1 (white) and RAGE (red). GFP^{+} (DP lineage) cells form both AT1
1225 cells (flattening; asterisk "*") and AT2 cells (MUC1^{+}) even upon *Cebpa* deletion. Bars, 25 µm. **d**
1226 Experimental design (top) and immunostains (bottom) for simultaneous *Cebpa* deletion and
1227 lineage labeling AT2 cells at PN11 via intraperitoneal (i.p.) tamoxifen (TMX) induction. Lungs
1228 were isolated 14 days post TMX (PN25) and immunostained for MUC1 (white) and RAGE

1229 (red). Alveolar regions of control *Sftpc*^{CreER}*; Rosa26*^{mTmG}*; Cebpa*$^{wt/fl}$ (left) and *Sftpc*^{CreER}*;*
1230 *Rosa26*^{mTmG}*; Cebpa*$^{fl/fl}$ (right) lungs immunostained as indicated, showing GFP$^+$/RAGE$^+$ AT1
1231 cells (asterisk) upon *Cebpa* deletion. Close up (bottom left) panels for each condition show a
1232 GFP$^+$/MUC1$^+$ AT2 (control; left) or GFP$^+$/RAGE$^+$ AT1 cell (*Cebpa* deletion; right). Bars, 100
1233 µm. **e** Quantification of (**d**) showing percent GFP$^+$ cells that differentiated into AT1s upon
1234 *Cebpa* deletion (n = 2856 GFP$^+$ cells sampled for control and 2105 for *Cebpa* deletion in
1235 experimental triplicate). ****$p = 6.4 \times 10^{-16}$ (Student's two-sided t-test, data as mean ± SD). All
1236 experiments were repeated at least three times. **f** Alveolar region of *Sftpc*^{CreER}*; Tg(iSuRe-Cre);*
1237 *Cebpa*$^{fl/fl}$ mouse lung immunostained for RAGE (white), RELMα (green) and Cre reporter (tdT).
1238 Lineage labeled RAGE$^+$ (arrowheads) and RELMα$^+$ (asterisk) cells are mutually exclusive from
1239 one another, showing the two distinct states upon loss of *Cebpa*.
1240

1241 **Supplementary Figure 5: *Cebpa* deletion and gene score validation.**
1242 **a** scRNAseq UMAP close-up of AT1 cluster (Figure 5a-i) depicting which cells are lineage
1243 positive (black) that converted to AT1s upon deletion of *Cebpa*. **b** Volcano plot showing
1244 downregulated (left) and upregulated (right) genes in AT2 cells upon *Cebpa* deletion. Genes are
1245 considered to have significant down/upregulation if $-\text{Log}_{10} P > 100$, and Log_2 fold change > 1 or
1246 < – 1 (red). **c** AT1 and AT2 gene score co-expression on scRNAseq UMAP of the developing
1247 lung[33] to assess changes in either AT2 or AT1 related genes. **d** nAT2 and mAT2 gene score co-
1248 expression on scRNAseq UMAP of the developing lung[33] to confirm restrictive expression of
1249 genes in either AT2 state. **e** AT1 and AT2 gene score (see Suppl. Table 1) co-expression on
1250 scRNAseq UMAP, showing retained AT2 gene score, and lack of an AT1 score upon loss of
1251 *Cebpa* in AT2 cells. **f** Alveolar regions of a PN25 *Sftpc*^{CreER}*; Tg(iSuRe-Cre)*mouse lung, 14 days

1252 after Cre induction with a sparse dose of TMX. Lungs were immunostained for MUC1 (green),
1253 tdT (red), and DAPI (blue). Bar, 25 µm. **g** Quantification of (**f**) for percent tdT^+ labeling of AT2
1254 cells in either sparse or high doses of TMX (n = 1258 AT2 cells sampled for high dose TMX and
1255 1670 for the sparse dose TMX). ****$p = 1.73 \times 10^{-9}$ (Student's two-sided t-test, data as
1256 mean ± SD). **h** Quantification of Figure 5b, showing percent tdT^+/EdU^+ proliferating cells upon
1257 *Cebpa* deletion in either High Dose or Sparse conditions. Note a significant reduction in
1258 proliferation upon sparse *Cebpa* deletion (n = 2358 tdT^+ cells sampled for the high dose deletion
1259 and 1115 for the sparse deletion in experimental triplicate). ****$p = 2.47 \times 10^{-9}$ (Student's two-
1260 sided t-test, data as mean ± SD). **i** Dot plot showing expression of the six genes (encoding for
1261 extracellular proteins) upregulated in the *Cebpa*$^{fl/fl}$ cluster, also enriched in nAT2 cells (Figure
1262 5d). **j** *Dlk1* gene expression on a scRNAseq developmental dataset confirming DLk1 expression
1263 in mAT2 cells. **k** Quantification of Lineage labeled organoids generated from AT2s isolated
1264 from *Sftpc*^{CreER}*; Tg(iSuRe-Cre); Cebpa*$^{wt/fl}$ and *Sftpc*^{CreER}*; Tg(iSuRe-Cre); Cebpa*$^{fl/fl}$ murine lung,
1265 showing higher percent $DLK1^+$ AT2s cells upon *Cebpa* deletion (n = 435 tdT^+ cells sampled for
1266 the *Cebpa* deletion and 435 for control in experimental triplicate). ****p = 0.0388 (Student's
1267 two-sided t-test). **l** Experimental design for labeling and deleting *Cebpa* in AT2 cells of *Sftpc-*
1268 *CreER;Tg(iSuRe-Cre);Cebpa*$^{wt/fl}$ and *Sftpc-CreER;Tg(iSuRe-Cre);Cebpa*$^{fl/fl}$ mice at PN11,
1269 isolating cells 14 days post TMX (at PN25) for scRNAseq and bulk ATACseq analyses. **m**
1270 Hierarchical clustering of sample binding sites shows high correlation between conditions in the
1271 ATAC-seq data. **n** Venn diagram of binding site overlaps in the ATAC-seq data between two
1272 programs for differential accessibility analysis – edgeR and DESeq2. **o** Differentially expressed
1273 gene (DEG) overlaps between RNA-seq and ATAC-seq data for the *Cebpa*$^{fl/fl}$ vs *Cebpa*$^{wt/fl}$ AT2
1274 cells. **p** Feature distribution from the ATAC-seq data detailing the genomic features associated

1275 with down- and upregulated binding sites upon loss of *Cebpa*. **q** HOMER analysis of the ATAC-
1276 seq data shows motifs enriched in the *Cebpa*$^{wt/fl}$ (red) and *Cebpa*$^{fl/fl}$ (blue). AP-1 and Yap/Taz
1277 interacting factors are highlighted via shape. **r** HOMER motifs and associated *p*-values highlight
1278 a role of AP1, TEAD, and NKX2.1 signaling in both the WT and KO conditions. **s** Schematic
1279 detailing the potential role of C/EBPα interacting with AP1 and NKX2.1 in AT2 (left) and AT1
1280 (right) cells.
1281
1282 **Supplementary Figure 6: Embryonic expression of C/EBPα and DLK1.**
1283 **a** Distal epithelial branch of an e17.5 lung immunostained for DLK1 (green), PDPN (red), and
1284 DAPI (blue). Bar, 10 µm. **b** Distal epithelial branch of an e15.5 lung immunostained for C/EBPα
1285 (green), PDPN (red), E-cadherin (ECAD, white), and DAPI (blue). No C/EBPα^{+} cells are
1286 detected in the distal epithelial branches at this point in development. Bar, 10 µm. **c** *Cebpa*
1287 (green) and *Ezh2* (red) co-expression on scRNAseq UMAP of the developing lung[33] shows
1288 mutually exclusive expression. **d** Analysis of ENCODE epigenetic dataset mapping of the PRC2
1289 modification H3K27me3 across developmental timepoints (e14.5 – P0) at the *Cebpa* locus. **e**
1290 Max normalized gene expression for *Cebpa* (red), *Dlk1* (green) and *Ezh2* (blue) during
1291 development from scRNAseq data of the developing lung[37], showing the relation of the
1292 components forming the I2-FFL that generates a pulse of *Dlk1*.**f** Dot plot showing expression of
1293 the Notch signaling pathway genes (ligands and its downstream activation) have distinct pattern
1294 as nascent cell fates are specified. **g** schematics of our working model how a Dlk1 pulse
1295 generator regulate AT2's accessibility to fate plasticity via Notch signaling.
1296
1297 **Supplementary Figure 7: AT2 defensive state and interferon signaling.**

1298 **a** Experimental design (top). 5 days after AAV-SPC-Cre (Control; left) or AAV-SPC-Cebpa-
1299 T2A-Cre (right) instillation into lungs of adult *Rosa26*^{mTmG} mice to induce constitutive GFP-Cre
1300 expression and overdrive expression of *Cebpa* in AT2 cells, lungs were injured by BHT (225
1301 mg/kg) intraperitoneal injection (i.p.). Lungs were isolated and immunostained for Cre reporter
1302 (GFP) and AT1 markers 14 days post injury (dpi). Immunostained images (bottom) show GFP$^+$
1303 AT1 cells (asterisk) in the control, but little to none when C/EBPα is overexpressed. Bars, 50
1304 μm. **b** Quantification of (**a**) for percent GFP$^+$ cells that differentiated into AT1 cells (n = 557
1305 GFP$^+$ cells sampled for the control condition and 631 for the *Cebpa* overdrive in experimental
1306 triplicate). ****$p = 6.5 \times 10^{-10}$ (Student's two-sided t-test, data as mean ± SD). **c** Immunostained
1307 adult lung showing GFP-labeling efficiency of AT2 cells (MUC1; white) by AAV-SPC-Cre
1308 (Figure 7a). Bar, 100 μm. **d** Dot plot showing interferon receptors (left) and interferon-γ target
1309 genes (right) for the AT2 clusters from the scRNAseq analysis. The AT2^{Def} cluster is highly
1310 enriched in both receptors and target genes. Interferon-γ specific receptor genes (dashed red box)
1311 are upregulated in the AT2^{Def} state upon loss of *Cebpa*. **e** Dot plot showing expression of DATP
1312 and Defender gene scores (top), along with expression of *Cebpa*, *Ezh2*, and DATP-associated
1313 genes (*Atf3*, *Atf4*, *Ddit3*) (bottom) in the clusters identified from the bleomycin injury timecourse
1314 scRNAseq dataset[20]. **f** DATP- and Defender-associated gene score co-expression shows a
1315 mutually exclusive pattern in four other lung injury model besides Cebpa deletion model (Fig 7j).
1316

Data Availability

The authors confirm that all relevant data are available in the paper or its Supplementary Information files. The scRNAseq datasets are available in the GEO repository under accession numbers "GSE119228", "GSE113320", "GSE109774", and "GSE149563" for developing and adult mouse lung cells, "GSE295269" for CEBP/α knockout mouse lung epithelial cells, "GSE141259" for adult bleomycin injury, "GSE218666" for AT1 injury, "GSE184384" for influenza injury, and "GSE113049" for LPS injury models. Source Data are available for this paper.

Code Availability

Code to reproduce the analyses described in this manuscript can be accessed at https://github.com/JimmyMayoGit/Sawhney_2025

Acknowledgments

The authors thank members of the Brownfield laboratory for helpful discussions and critical reading of the manuscript. We thank D. Tenen (*Cebpa*$^{fl/fl}$) for the transgenic mouse strain; Hannah Golding for performing organotypic culture experiments; and Gamaliel Taengwa for data quantification. This work was supported by R00HL127267, R01HL171056, and a Pilot Award from Mayo Clinic's Center for Biomedical Discovery (D.G.B).

Author Contributions

ASS, BJD, and DGB conceived the study and designed the experiments. ASS, BJD, JC, DG, GA, AO, HH, LS, XQ, SRH, ASU performed the experiments. ASS, BJD, and AO analyzed and

interpreted the data. JC, AH, EL, and DGB performed the scRNAseq analysis. DG and ZW performed the ATACseq analysis. RW and SD performed bleomycin injury experiments, and KAS and ZI performed BH3 profiling experiments. DGB, ASS, and BJD wrote the paper.

Ethics Declarations

Competing interests

The authors have no competing interests to declare.

1348 **References:**

1349 1. Barnes PJ*, et al.* Chronic obstructive pulmonary disease. *Nat Rev Dis Primers* **1**, 15076
1350 (2015).

1351
1352 2. Martinez FJ*, et al.* Idiopathic pulmonary fibrosis. *Nature Rev Dis Primers* **3**, 17074 (2017).

1353
1354 3. Siegel R, Naishadham D, Jemal A. Cancer statistics, 2013. *CA Cancer J Clin* **63**, 11-30
1355 (2013).

1356
1357 4. Desai TJ, Brownfield DG, Krasnow MA. Alveolar progenitor and stem cells in lung
1358 development, renewal and cancer. *Nature* **507**, 190-194 (2014).

1359
1360 5. Franks TJ*, et al.* Lung pathology of severe acute respiratory syndrome (SARS): a study of
1361 8 autopsy cases from Singapore. *Hum Pathol* **34**, 743-748 (2003).

1362
1363 6. Hwang DM, Chamberlain DW, Poutanen SM, Low DE, Asa SL, Butany J. Pulmonary
1364 pathology of severe acute respiratory syndrome in Toronto. *Mod Pathol* **18**, 1-10 (2005).

1365
1366 7. Tian S, Hu W, Niu L, Liu H, Xu H, Xiao SY. Pulmonary pathology of early-phase 2019 novel
1367 coronavirus (COVID-19) pneumonia in two patients with lung cancer. *J Thorac Oncol* **15**,
1368 700-704 (2020).

1369
1370 8. Rawlins EL, Clark CP, Xue Y, Hogan BL. The Id2+ distal tip lung epithelium contains
1371 individual multipotent embryonic progenitor cells. *Development* **136**, 3741-3745 (2009).

1372
1373 9. Treutlein B*, et al.* Reconstructing lineage hierarchies of the distal lung epithelium using
1374 single-cell RNA-seq. *Nature* **509**, 371-375 (2014).

1375
1376 10. Brownfield DG, de Arce AD, Ghelfi E, Gillich A, Desai TJ, Krasnow MA. Alveolar cell fate
1377 selection and lifelong maintenance of AT2 cells by FGF signaling. *Nat Commun* **13**, 7137
1378 (2022).

1379
1380 11. Zacharias WJ*, et al.* Regeneration of the lung alveolus by an evolutionarily conserved
1381 epithelial progenitor. *Nature* **555**, 251-255 (2018).

1382

1383 12. Frank DB*, et al.* Early lineage specification defines alveolar epithelial ontogeny in the
1384 murine lung. *Proc Natl Acad Sci U S A* **116**, 4362-4371 (2019).

1385
1386 13. Vila Ellis L, Chen J. A cell-centric view of lung alveologenesis. *Dev Dyn* **250**, 482-496
1387 (2021).

1388
1389 14. Weibel ER. On the tricks alveolar epithelial cells play to make a good lung. *Am J Respir*
1390 *Crit Care Med* **191**, 504-513 (2015).

1391
1392 15. Shenoy AT*, et al.* Antigen presentation by lung epithelial cells directs CD4+ TRM cell
1393 function and regulates barrier immunity. *Nature Communications* **12**, 5834 (2021).

1394
1395 16. Choi J*, et al.* Inflammatory Signals Induce AT2 Cell-Derived Damage-Associated Transient
1396 Progenitors that Mediate Alveolar Regeneration. *Cell Stem Cell* **27**, 366-382 e367 (2020).

1397
1398 17. Malik A*, et al.* Epithelial IFNγ signalling and compartmentalized antigen presentation
1399 orchestrate gut immunity. *Nature* **623**, 1044-1052 (2023).

1400
1401 18. Gessani S, Conti L, Del Cornò M, Belardelli F. Type I interferons as regulators of human
1402 antigen presenting cell functions. *Toxins (Basel)* **6**, 1696-1723 (2014).

1403
1404 19. Rock JR*, et al.* Multiple stromal populations contribute to pulmonary fibrosis without
1405 evidence for epithelial to mesenchymal transition. *Proc Natl Acad Sci U S A* **108**, E1475-
1406 1483 (2011).

1407
1408 20. Strunz M*, et al.* Alveolar regeneration through a Krt8+ transitional stem cell state that
1409 persists in human lung fibrosis. *Nat Commun* **11**, 3559 (2020).

1410
1411 21. Barkauskas CE*, et al.* Type 2 alveolar cells are stem cells in adult lung. *The Journal of*
1412 *clinical investigation* **123**, 3025-3036 (2013).

1413
1414 22. Nabhan AN, Brownfield DG, Harbury PB, Krasnow MA, Desai TJ. Single-cell Wnt signaling
1415 niches maintain stemness of alveolar type 2 cells. *Science* **359**, 1118-1123 (2018).

1416

1417 23. Finn J*, et al.* Dlk1-Mediated Temporal Regulation of Notch Signaling Is Required for
1418 Differentiation of Alveolar Type II to Type I Cells during Repair. *Cell Rep* **26**, 2942-2954
1419 e2945 (2019).

1420
1421 24. Major J*, et al.* Type I and III interferons disrupt lung epithelial repair during recovery
1422 from viral infection. *Science* **369**, 712-717 (2020).

1423
1424 25. Jiang P*, et al.* Ineffectual Type 2-to-Type 1 Alveolar Epithelial Cell Differentiation in
1425 Idiopathic Pulmonary Fibrosis: Persistence of the KRT8(hi) Transitional State. *Am J Respir*
1426 *Crit Care Med* **201**, 1443-1447 (2020).

1427
1428 26. Lourenco AR*, et al.* C/EBPa is crucial determinant of epithelial maintenance by
1429 preventing epithelial-to-mesenchymal transition. *Nat Commun* **11**, 785 (2020).

1430
1431 27. Suh HC, Gooya J, Renn K, Friedman AD, Johnson PF, Keller JR. C/EBPalpha determines
1432 hematopoietic cell fate in multipotential progenitor cells by inhibiting erythroid
1433 differentiation and inducing myeloid differentiation. *Blood* **107**, 4308-4316 (2006).

1434
1435 28. Baladron V*, et al.* dlk acts as a negative regulator of Notch1 activation through
1436 interactions with specific EGF-like repeats. *Exp Cell Res* **303**, 343-359 (2005).

1437
1438 29. Grassi ES, Pietras A. Emerging Roles of DLK1 in the Stem Cell Niche and Cancer
1439 Stemness. *J Histochem Cytochem* **70**, 17-28 (2022).

1440
1441 30. Yen YP*, et al.* Dlk1-Dio3 locus-derived lncRNAs perpetuate postmitotic motor neuron cell
1442 fate and subtype identity. *Elife* **7**, (2018).

1443
1444 31. Zhao J*, et al.* PPARgamma and C/EBPalpha enable adipocyte differentiation upon
1445 inhibition of histone methyltransferase PRC2 in malignant tumors. *J Biol Chem* **300**,
1446 107765 (2024).

1447
1448 32. Auyeung VC*, et al.* IRE1alpha drives lung epithelial progenitor dysfunction to establish a
1449 niche for pulmonary fibrosis. *Am J Physiol Lung Cell Mol Physiol* **322**, L564-L580 (2022).

1450
1451 33. Cohen M*, et al.* Lung single-cell signaling interaction map reveals basophil role in
1452 macrophage imprinting. *Cell* **175**, 1031-1044 e1018 (2018).

1453
1454 34. Gillich A, St. Julien KR, Brownfield DG, Travaglini KJ, Metzger RJ, Krasnow MA. Alveoli
1455 form directly by budding led by a single epithelial cell. *bioRxiv*, 2021.2012.2025.474174
1456 (2021).

1457
1458 35. Blanco MA*, et al.* Chromatin-state barriers enforce an irreversible mammalian cell fate
1459 decision. *Cell Reports* **37**, 109967 (2021).

1460
1461 36. Hurley K*, et al.* Reconstructed Single-Cell Fate Trajectories Define Lineage Plasticity
1462 Windows during Differentiation of Human PSC-Derived Distal Lung Progenitors. *Cell*
1463 *Stem Cell* **26**, 593-608.e598 (2020).

1464
1465 37. Zepp JA*, et al.* Genomic, epigenomic, and biophysical cues controlling the emergence of
1466 the lung alveolus. *Science* **371**, (2021).

1467
1468 38. Sarosiek KA*, et al.* Developmental Regulation of Mitochondrial Apoptosis by c-Myc
1469 Governs Age- and Tissue-Specific Sensitivity to Cancer Therapeutics. *Cancer Cell* **31**, 142-
1470 156 (2017).

1471
1472 39. Singh R*, et al.* Radiotherapy-Induced Neurocognitive Impairment Is Driven by
1473 Heightened Apoptotic Priming in Early Life and Prevented by Blocking BAX. *Cancer Res*
1474 **83**, 3442-3461 (2023).

1475
1476 40. Basundra R*, et al.* Constitutive High Expression of NOXA Sensitizes Human Embryonic
1477 Stem Cells for Rapid Cell Death. *Stem Cells* **40**, 49-58 (2022).

1478
1479 41. A single-cell transcriptomic atlas characterizes ageing tissues in the mouse. *Nature* **583**,
1480 590-595 (2020).

1481
1482 42. Zhang Z*, et al.* Transcription factor Etv5 is essential for the maintenance of alveolar type
1483 II cells. *Proc Natl Acad Sci U S A* **114**, 3903-3908 (2017).

1484
1485 43. Metzger DE, Stahlman MT, Shannon JM. Misexpression of ELF5 disrupts lung branching
1486 and inhibits epithelial differentiation. *Dev Biol* **320**, 149-160 (2008).

1487
1488 44. Santofimia-Castaño P*, et al.* Inactivation of NUPR1 promotes cell death by coupling ER-
1489 stress responses with necrosis. *Sci Rep* **8**, 16999 (2018).

1490
1491 45. Liu J*, et al.* NUPR1 is a critical repressor of ferroptosis. *Nature Communications* **12**, 647
1492 (2021).

1493
1494 46. Basseres DS*, et al.* Respiratory failure due to differentiation arrest and expansion of
1495 alveolar cells following lung-specific loss of the transcription factor C/EBPalpha in mice.
1496 *Mol Cell Biol* **26**, 1109-1123 (2006).

1497
1498 47. Martis PC, Whitsett JA, Xu Y, Perl AK, Wan H, Ikegami M. C/EBPalpha is required for lung
1499 maturation at birth. *Development* **133**, 1155-1164 (2006).

1500
1501 48. Morimoto M, Kopan R. rtTA toxicity limits the usefulness of the SP-C-rtTA transgenic
1502 mouse. *Dev Biol* **325**, 171-178 (2009).

1503
1504 49. Fernández-Chacón M*, et al.* iSuRe-Cre is a genetic tool to reliably induce and report Cre-
1505 dependent genetic modifications. *Nat Commun* **10**, 2262 (2019).

1506
1507 50. Germani F, Bergantinos C, Johnston LA. Mosaic Analysis in Drosophila. *Genetics* **208**,
1508 473-490 (2018).

1509
1510 51. Burke R, Basler K. Dpp receptors are autonomously required for cell proliferation in the
1511 entire developing Drosophila wing. *Development* **122**, 2261-2269 (1996).

1512
1513 52. Hassan D, Chen J. CEBPA restricts alveolar type 2 cell plasticity during development and
1514 injury-repair. *Nat Commun* **15**, 4148 (2024).

1515
1516 53. Nueda ML, Baladrón V, Sánchez-Solana B, Ballesteros MA, Laborda J. The EGF-like
1517 protein dlk1 inhibits notch signaling and potentiates adipogenesis of mesenchymal cells.
1518 *J Mol Biol* **367**, 1281-1293 (2007).

1519
1520 54. Ramji DP, Foka P. CCAAT/enhancer-binding proteins: structure, function and regulation.
1521 *Biochem J* **365**, 561-575 (2002).

1522
1523 55. Little DR, Lynch AM, Yan Y, Akiyama H, Kimura S, Chen J. Differential chromatin binding
1524 of the lung lineage transcription factor NKX2-1 resolves opposing murine alveolar cell
1525 fates in vivo. *Nat Commun* **12**, 2509 (2021).

1526
1527 56. Aronson BE*, et al.* A bipartite element with allele-specific functions safeguards DNA
1528 methylation imprints at the Dlk1-Dio3 locus. *Dev Cell* **56**, 3052-3065.e3055 (2021).

1529
1530 57. Hagan JP, O'Neill BL, Stewart CL, Kozlov SV, Croce CM. At least ten genes define the
1531 imprinted Dlk1-Dio3 cluster on mouse chromosome 12qF1. *PLoS One* **4**, e4352 (2009).

1532
1533 58. Visel A, Thaller C, Eichele G. GenePaint.org: an atlas of gene expression patterns in the
1534 mouse embryo. *Nucleic Acids Res* **32**, D552-556 (2004).

1535
1536 59. Sanli I*, et al.* Meg3 Non-coding RNA Expression Controls Imprinting by Preventing
1537 Transcriptional Upregulation in cis. *Cell Reports* **23**, 337-348 (2018).

1538
1539 60. He Y*, et al.* Spatiotemporal DNA methylome dynamics of the developing mouse fetus.
1540 *Nature* **583**, 752-759 (2020).

1541
1542 61. Zheng R*, et al.* Cistrome Data Browser: expanded datasets and new tools for gene
1543 regulatory analysis. *Nucleic Acids Research* **47**, D729-D735 (2018).

1544
1545 62. Alon U. *An introduction to systems biology : design principles of biological circuits*,
1546 Second edition. edn. CRC Press, Taylor & Francis Group (2020).

1547
1548 63. Chitnis AB. The role of Notch in lateral inhibition and cell fate specification. *Mol Cell*
1549 *Neurosci* **6**, 311-321 (1995).

1550
1551 64. Ochi S, Imaizumi Y, Shimojo H, Miyachi H, Kageyama R. Oscillatory expression of Hes1
1552 regulates cell proliferation and neuronal differentiation in the embryonic brain.
1553 *Development* **147**, (2020).

1554
1555 65. Nueda ML, Naranjo AI, Baladron V, Laborda J. The proteins DLK1 and DLK2 modulate
1556 NOTCH1-dependent proliferation and oncogenic potential of human SK-MEL-2
1557 melanoma cells. *Biochim Biophys Acta* **1843**, 2674-2684 (2014).

1558
1559 66. Milara J*, et al.* Sphingosine-1-phosphate is increased in patients with idiopathic
1560 pulmonary fibrosis and mediates epithelial to mesenchymal transition. *Thorax* **67**, 147-
1561 156 (2012).

67. Kobayashi Y*, et al.* Persistence of a regeneration-associated, transitional alveolar epithelial cell state in pulmonary fibrosis. *Nat Cell Biol* **22**, 934-946 (2020).

68. Jiang HY*, et al.* Activating transcription factor 3 is integral to the eukaryotic initiation factor 2 kinase stress response. *Mol Cell Biol* **24**, 1365-1377 (2004).

69. Ma Y, Brewer JW, Diehl JA, Hendershot LM. Two distinct stress signaling pathways converge upon the CHOP promoter during the mammalian unfolded protein response. *J Mol Biol* **318**, 1351-1365 (2002).

70. Ron D, Habener JF. CHOP, a novel developmentally regulated nuclear protein that dimerizes with transcription factors C/EBP and LAP and functions as a dominant-negative inhibitor of gene transcription. *Genes Dev* **6**, 439-453 (1992).

71. Konkimalla A*, et al.* Transitional cell states sculpt tissue topology during lung regeneration. *Cell Stem Cell* **30**, 1486-1502 e1489 (2023).

72. Beppu AK*, et al.* Epithelial plasticity and innate immune activation promote lung tissue remodeling following respiratory viral infection. *Nat Commun* **14**, 5814 (2023).

73. Riemondy KA*, et al.* Single cell RNA sequencing identifies TGFbeta as a key regenerative cue following LPS-induced lung injury. *JCI Insight* **5**, (2019).

74. Goss AM*, et al.* Wnt2/2b and beta-catenin signaling are necessary and sufficient to specify lung progenitors in the foregut. *Dev Cell* **17**, 290-298 (2009).

75. Li J, Wang Z, Chu Q, Jiang K, Li J, Tang N. The strength of mechanical forces determines the differentiation of alveolar epithelial cells. *Dev Cell* **44**, 297-312 e295 (2018).

76. Konkimalla A*, et al.* Multi-apical polarity of alveolar stem cells and their dynamics during lung development and regeneration. *iScience* **25**, 105114 (2022).

77. Alanis DM, Chang DR, Akiyama H, Krasnow MA, Chen J. Two nested developmental waves demarcate a compartment boundary in the mouse lung. *Nat Commun* **5**, 3923 (2014).

1598
1599 78. Inde Z*, et al.* Age-dependent regulation of SARS-CoV-2 cell entry genes and cell death
1600 programs correlates with COVID-19 severity. *Sci Adv* **7**, (2021).

1601
1602 79. Penkala IJ*, et al.* Age-dependent alveolar epithelial plasticity orchestrates lung
1603 homeostasis and regeneration. *Cell Stem Cell* **28**, 1775-1789 e1775 (2021).

1604
1605 80. Sprinzak D*, et al.* Cis-interactions between Notch and Delta generate mutually exclusive
1606 signalling states. *Nature* **465**, 86-90 (2010).

1607
1608 81. Kagami M*, et al.* The IG-DMR and the MEG3-DMR at human chromosome 14q32.2:
1609 hierarchical interaction and distinct functional properties as imprinting control centers.
1610 *PLoS Genet* **6**, e1000992 (2010).

1611
1612 82. Yao C*, et al.* Senescence of Alveolar Type 2 Cells Drives Progressive Pulmonary Fibrosis.
1613 *Am J Respir Crit Care Med* **203**, 707-717 (2021).

1614
1615 83. Wang F*, et al.* Regulation of epithelial transitional states in murine and human
1616 pulmonary fibrosis. *The Journal of clinical investigation* **133**, (2023).

1617
1618 84. Kaufman RJ. Stress signaling from the lumen of the endoplasmic reticulum: coordination
1619 of gene transcriptional and translational controls. *Genes Dev* **13**, 1211-1233 (1999).

1620
1621 85. Toth A*, et al.* Alveolar epithelial progenitor cells require Nkx2-1 to maintain progenitor-
1622 specific epigenomic state during lung homeostasis and regeneration. *Nature*
1623 *Communications* **14**, 8452 (2023).

1624
1625 86. Zhang P*, et al.* Enhancement of hematopoietic stem cell repopulating capacity and self-
1626 renewal in the absence of the transcription factor C/EBP alpha. *Immunity* **21**, 853-863
1627 (2004).

1628
1629 87. Shen X*, et al.* EZH1 mediates methylation on histone H3 lysine 27 and complements
1630 EZH2 in maintaining stem cell identity and executing pluripotency. *Mol Cell* **32**, 491-502
1631 (2008).

1632
1633 88. Muzumdar MD, Tasic B, Miyamichi K, Li L, Luo L. A global double-fluorescent Cre
1634 reporter mouse. *Genesis* **45**, 593-605 (2007).

1635
1636 89. Wolf FA, Angerer P, Theis FJ. SCANPY: large-scale single-cell gene expression data
1637 analysis. *Genome Biol* **19**, 15 (2018).

1638
1639 90. Hao Y*, et al.* Integrated analysis of multimodal single-cell data. *Cell* **184**, 3573-
1640 3587.e3529 (2021).

1641
1642 91. McGinnis CS, Murrow LM, Gartner ZJ. DoubletFinder: Doublet Detection in Single-Cell
1643 RNA Sequencing Data Using Artificial Nearest Neighbors. *Cell Syst* **8**, 329-337.e324
1644 (2019).

1645
1646 92. Haber AL*, et al.* A single-cell survey of the small intestinal epithelium. *Nature* **551**, 333-
1647 339 (2017).

1648
1649 93. La Manno G*, et al.* RNA velocity of single cells. *Nature* **560**, 494-498 (2018).

1650
1651 94. Wolf FA*, et al.* PAGA: graph abstraction reconciles clustering with trajectory inference
1652 through a topology preserving map of single cells. *Genome Biology* **20**, 59 (2019).

1653
1654 95. Bergen V, Lange M, Peidli S, Wolf FA, Theis FJ. Generalizing RNA velocity to transient cell
1655 states through dynamical modeling. *Nat Biotechnol* **38**, 1408-1414 (2020).

1656
1657 96. Wagner DE, Weinreb C, Collins ZM, Briggs JA, Megason SG, Klein AM. Single-cell
1658 mapping of gene expression landscapes and lineage in the zebrafish embryo. *Science*
1659 **360**, 981-987 (2018).

1660
1661 97. Heinz S*, et al.* Simple combinations of lineage-determining transcription factors prime
1662 cis-regulatory elements required for macrophage and B cell identities. *Mol Cell* **38**, 576-
1663 589 (2010).

1664
1665 98. Gontarz P*, et al.* Comparison of differential accessibility analysis strategies for ATAC-seq
1666 data. *Sci Rep* **10**, 10150 (2020).

1667
1668 99. Love MI, Huber W, Anders S. Moderated estimation of fold change and dispersion for
1669 RNA-seq data with DESeq2. *Genome Biol* **15**, 550 (2014).

1670

1671 100. Mei S*, et al.* Cistrome Data Browser: a data portal for ChIP-Seq and chromatin
1672 accessibility data in human and mouse. *Nucleic Acids Research* **45**, D658-D662 (2016).

1673
1674 101. Lei Y, He L, Yan C, Wang Y, Lv G. PERK activation by CCT020312 chemosensitizes
1675 colorectal cancer through inducing apoptosis regulated by ER stress. *Biochem Biophys*
1676 *Res Commun* **557**, 316-322 (2021).

1677

1678

Figure 1, Sawhney-Deskin et al.

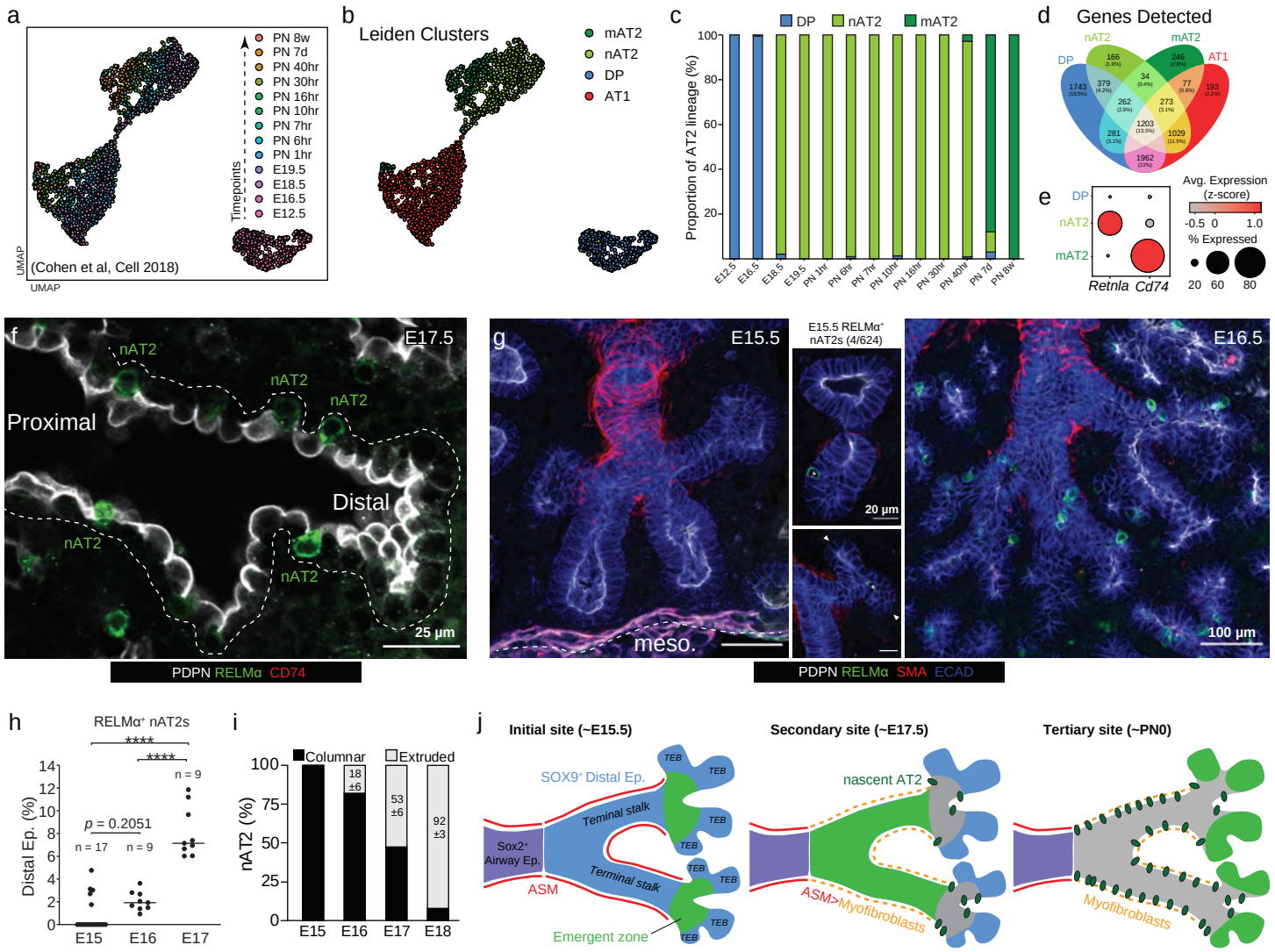

Figure 2, Sawhney-Deskin et al.

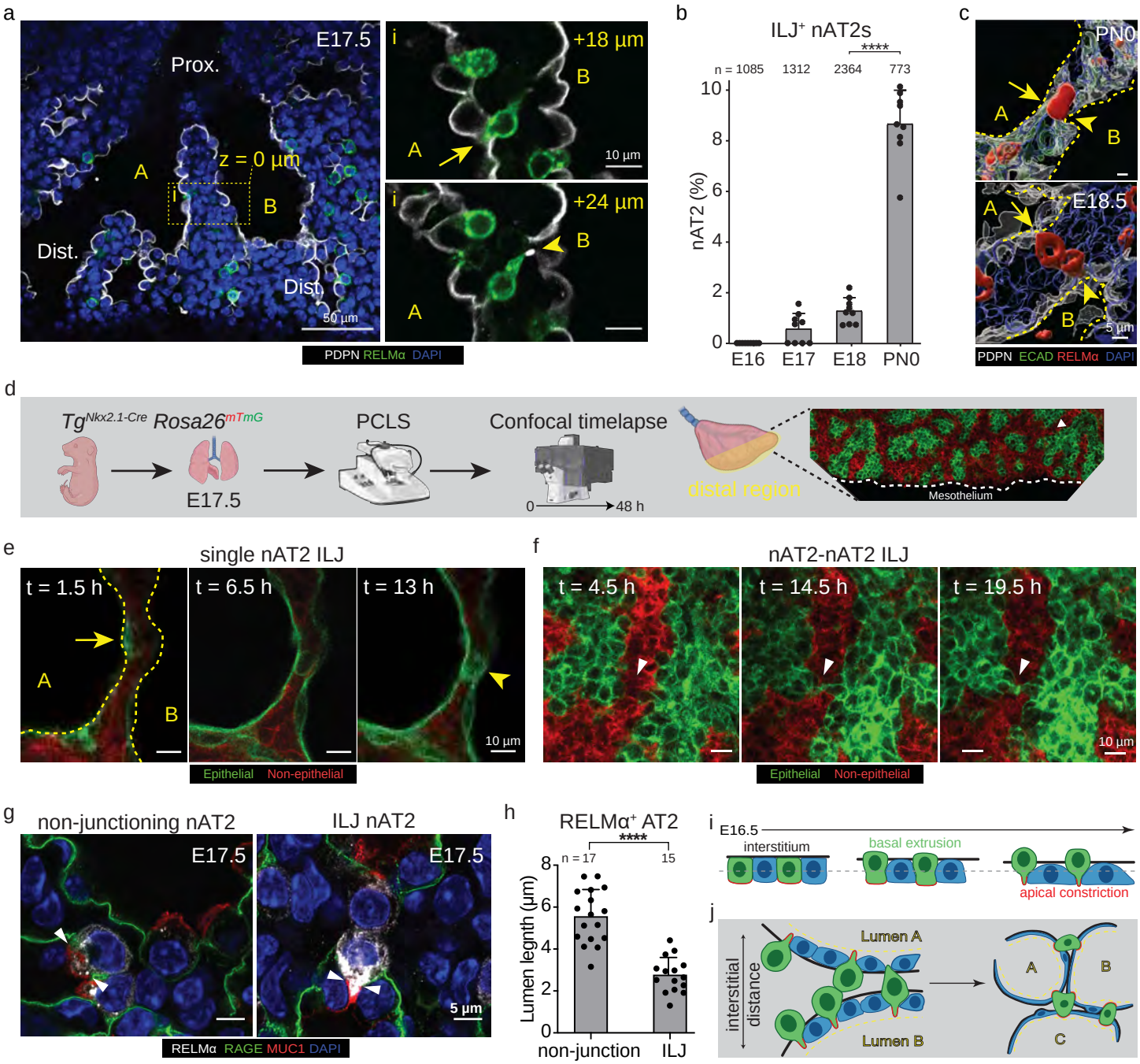

Figure 3, Sawhney-Deskin et al.

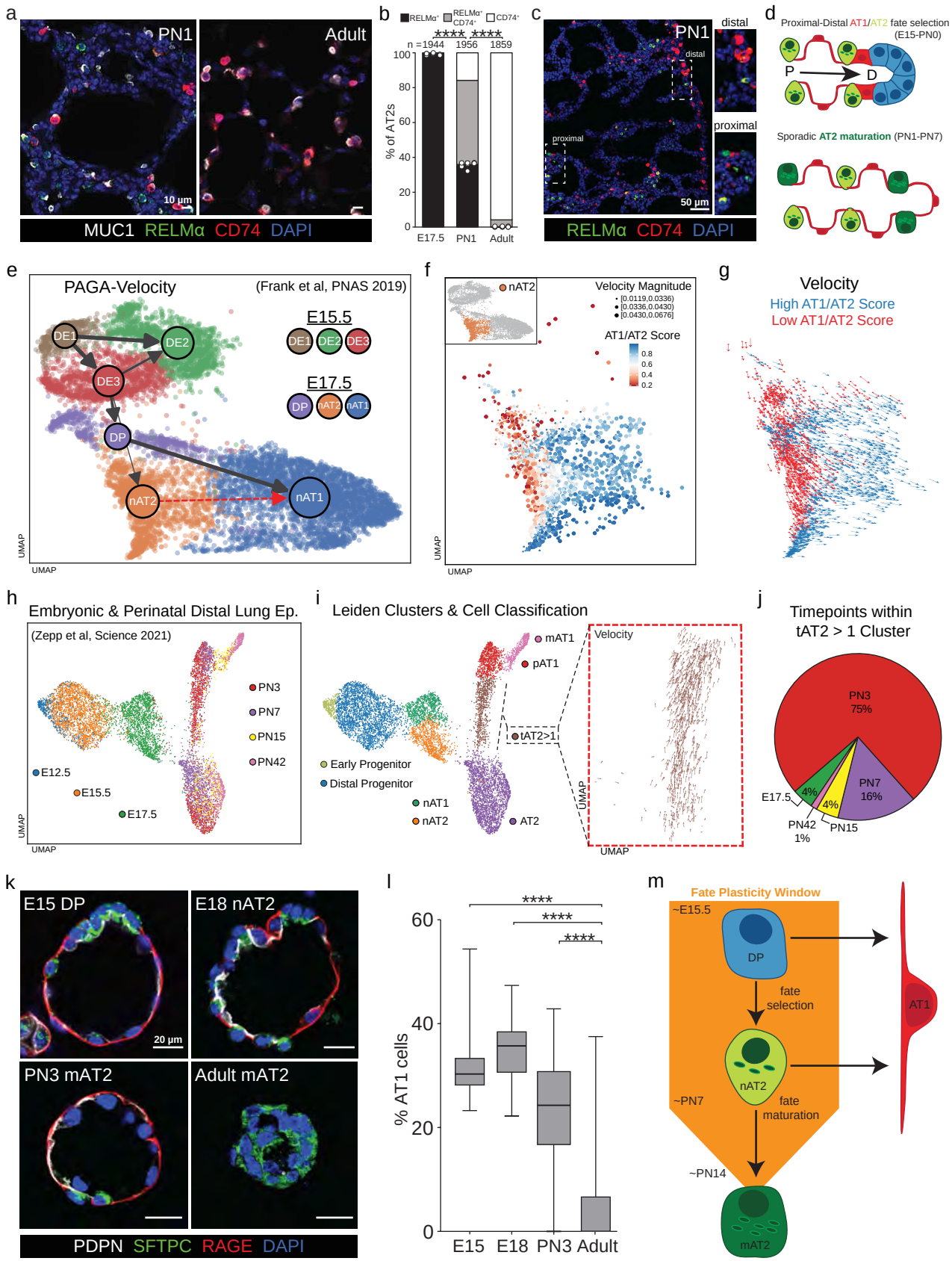

Figure 4, Sawhney-Deskin et al.

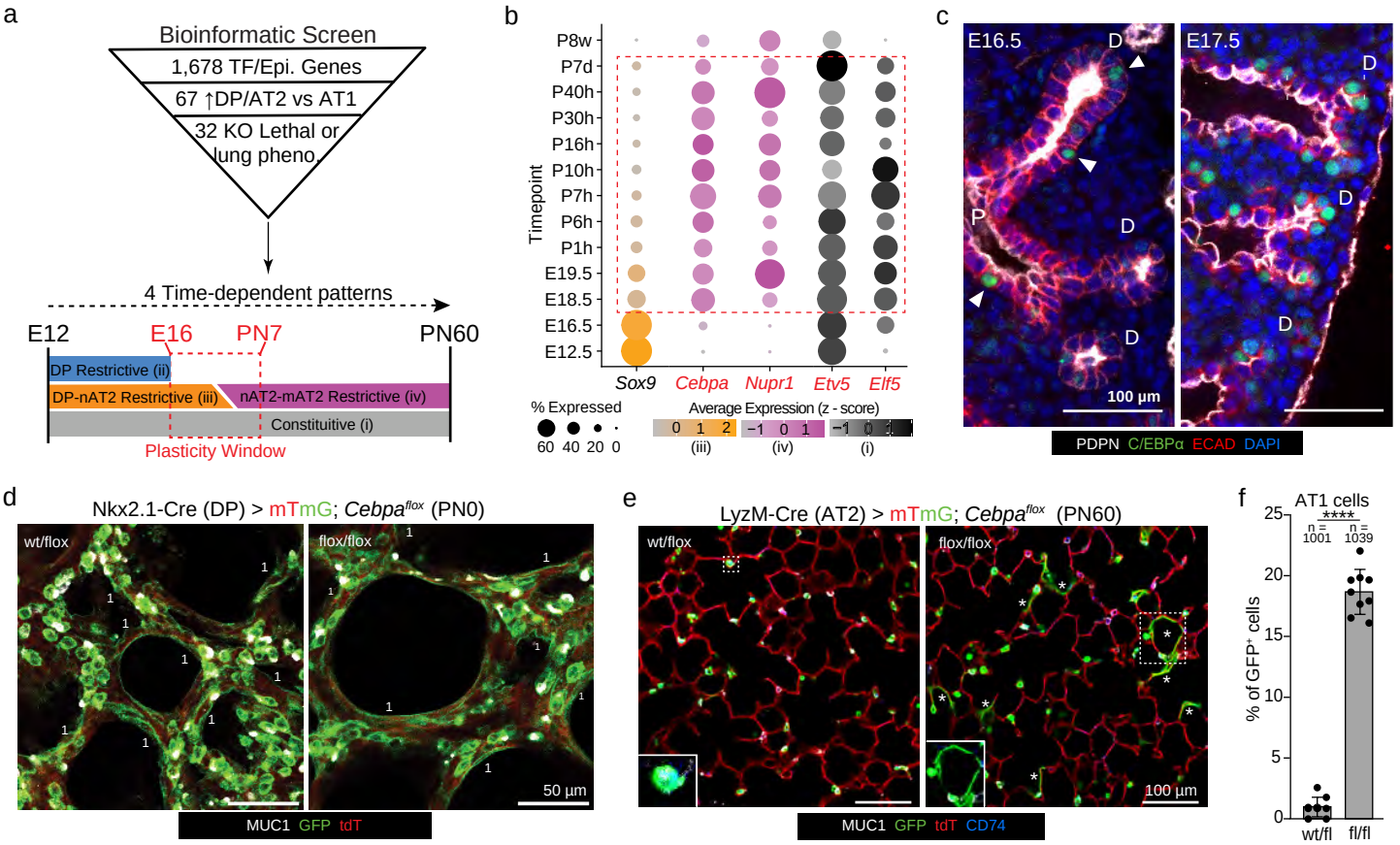

Figure 5, Sawhney-Deskin et al.

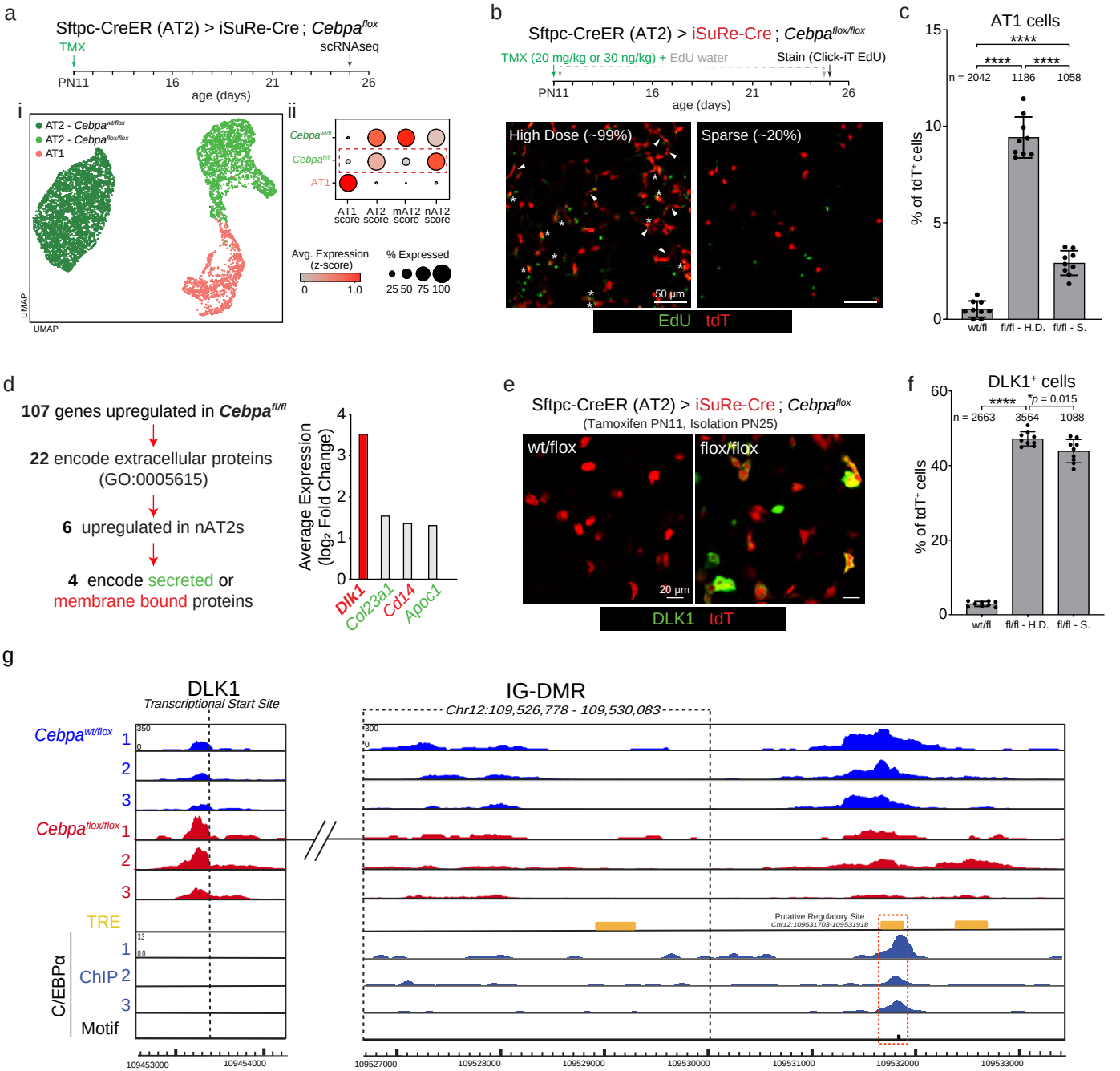

Figure 6, Sawhney-Deskin et al.

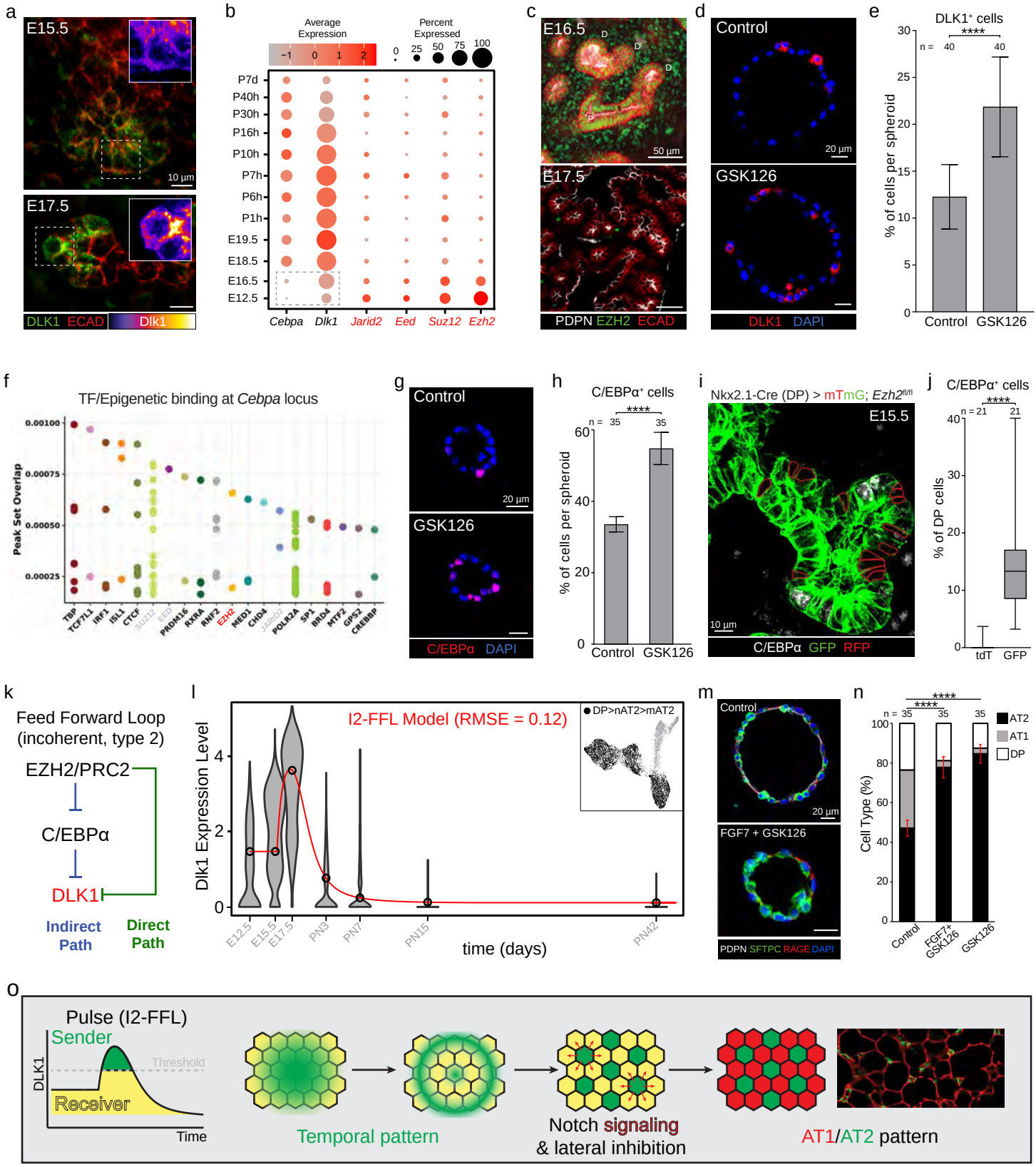

Figure 7, Sawhney-Deskin et al.

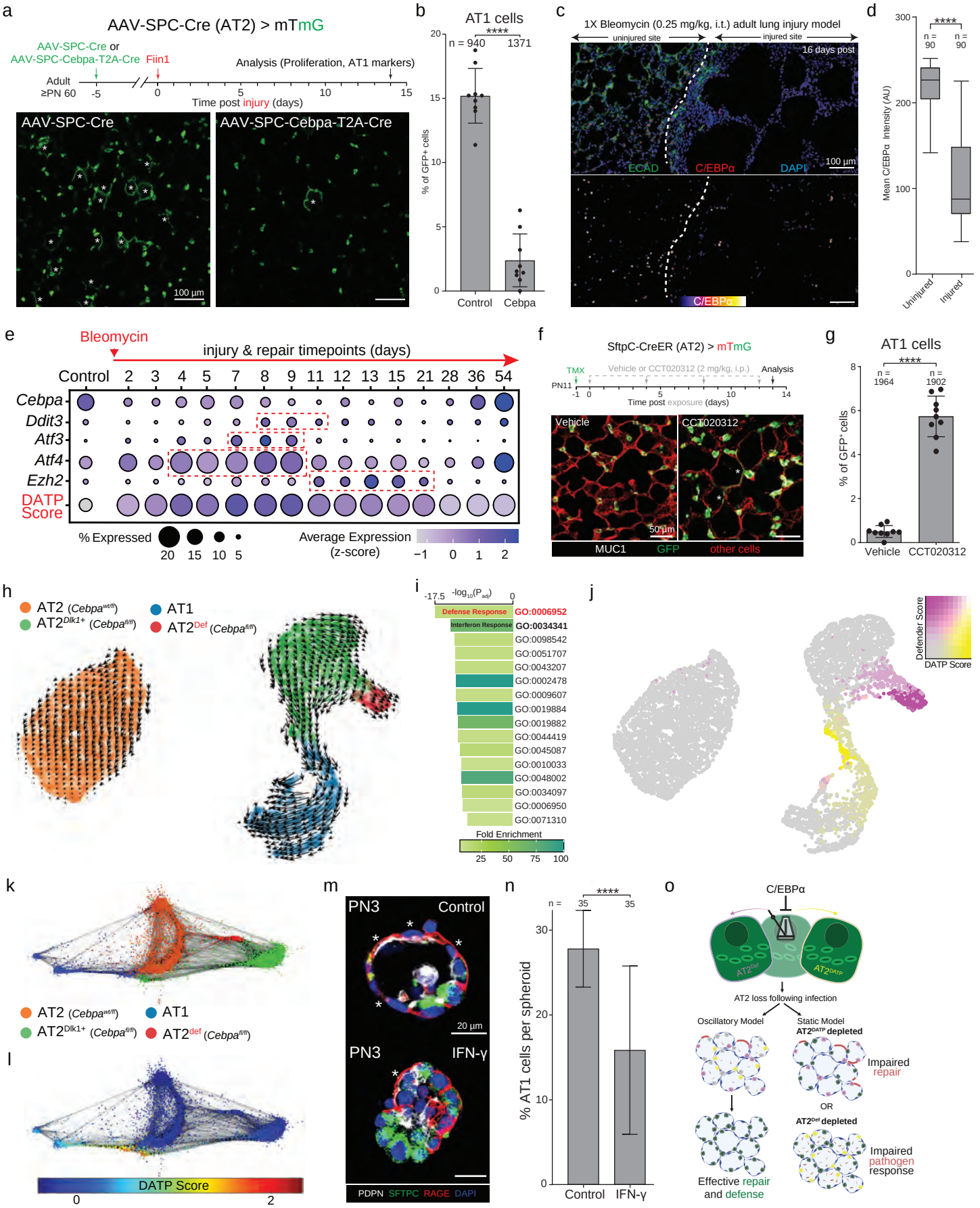

Supplementary Figure 1, Sawhney-Deskin et al.

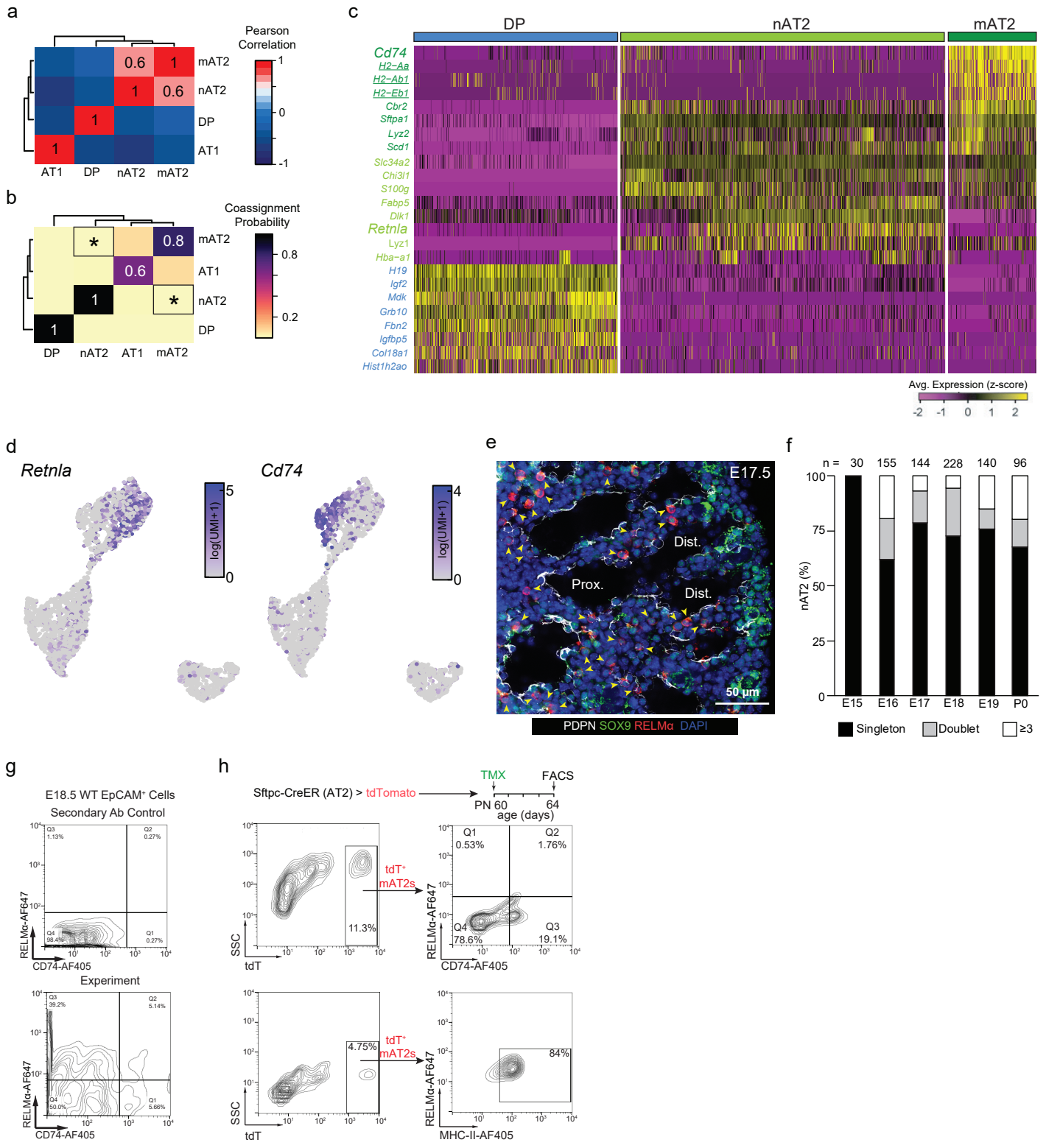

Supplementary Figure 2, Sawhney-Deskin et al.

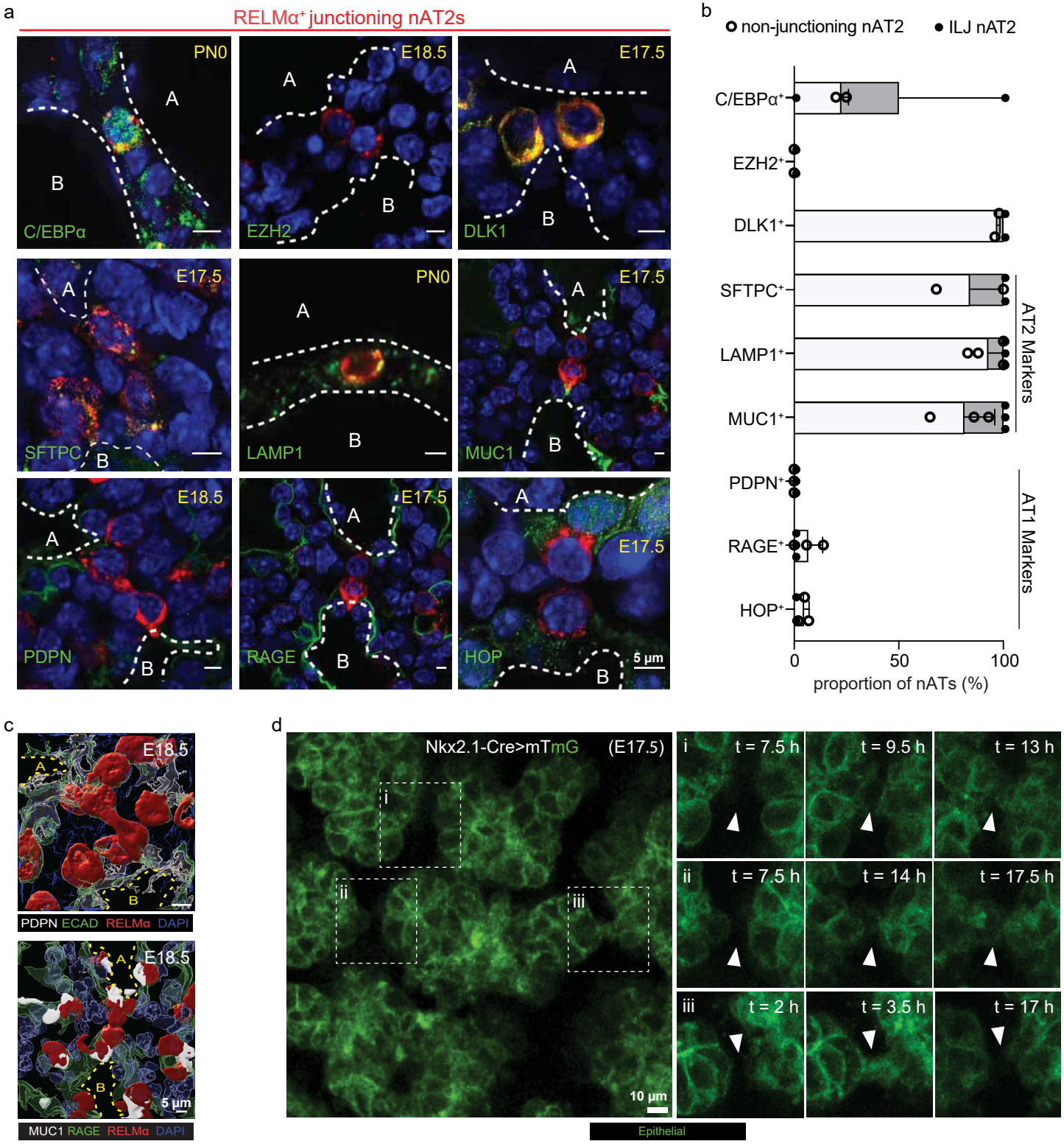

Supplementary Figure 3, Sawhney-Deskin et al.

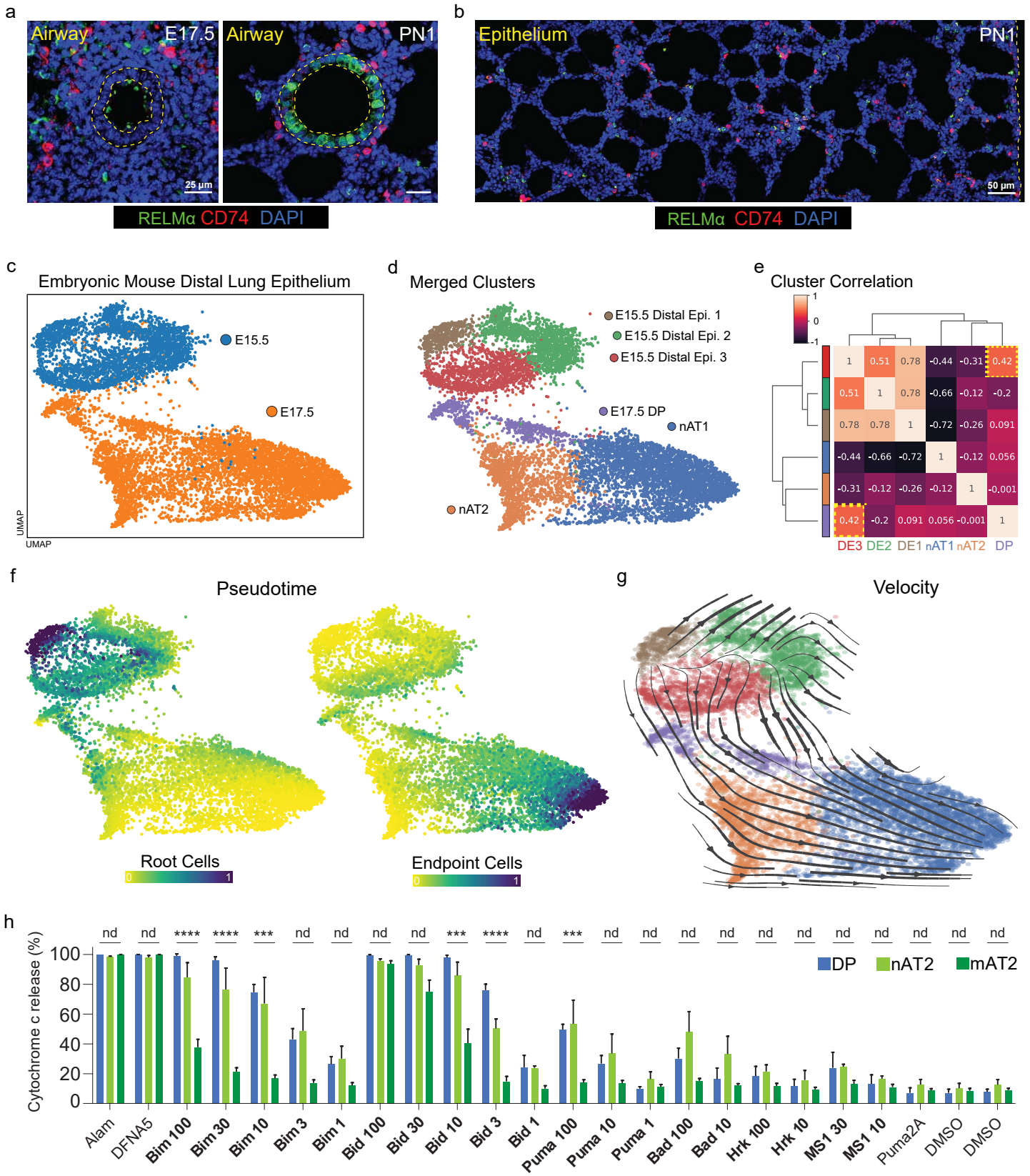

Supplementary Figure 4, Sawhney-Deskin et al.

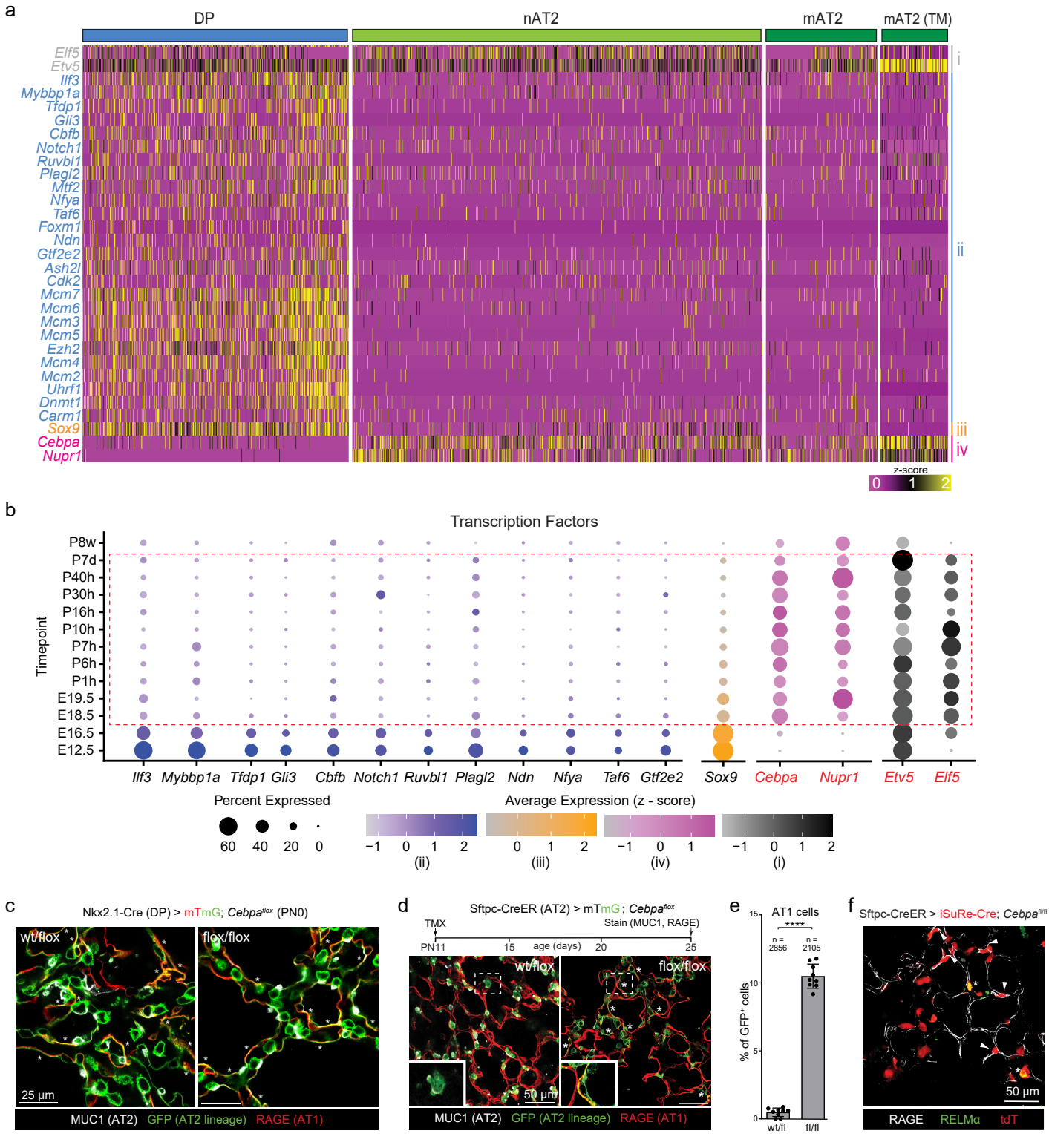

Supplementary Figure 5, Sawhney-Deskin et al.

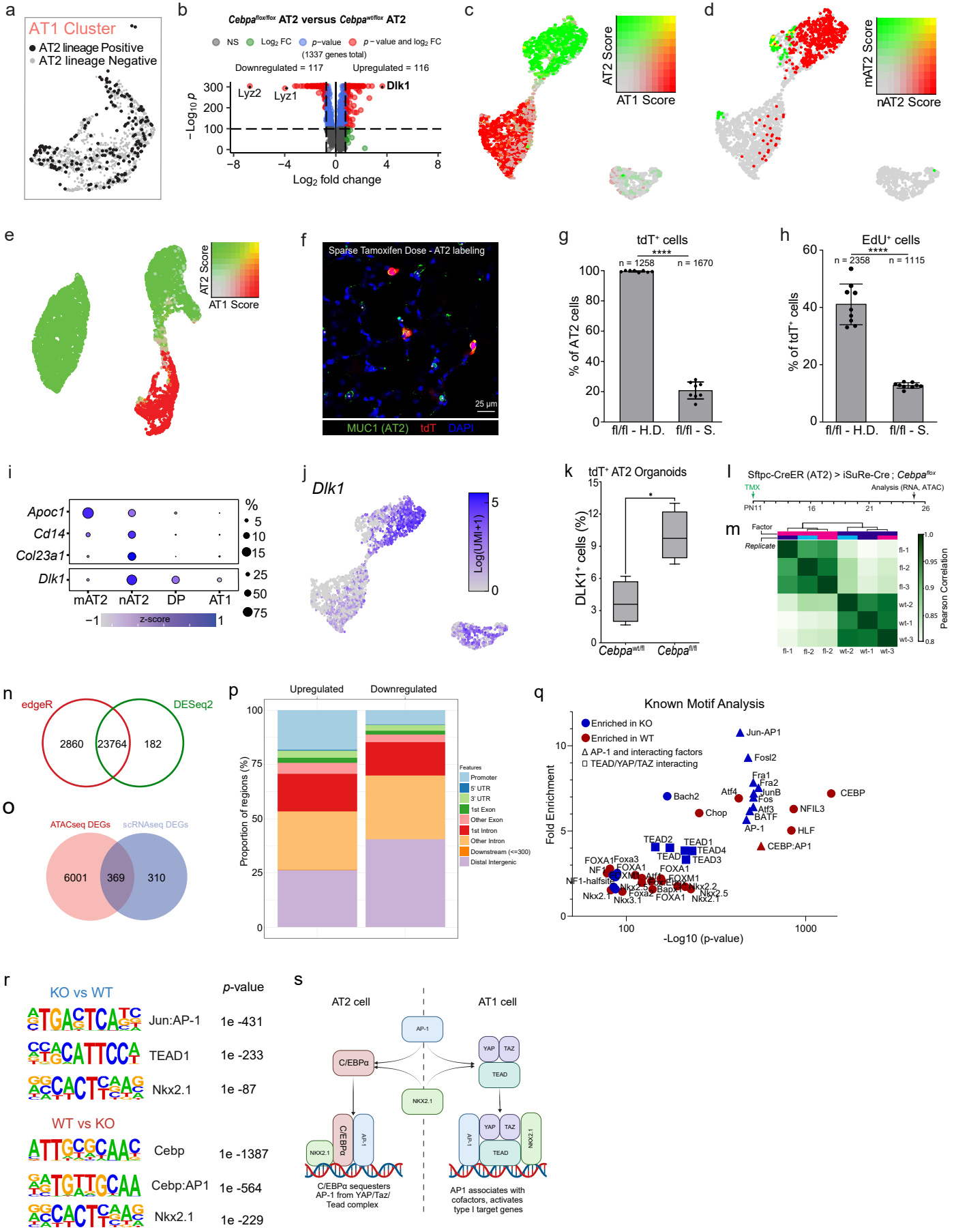

Supplementary Figure 6, Sawhney-Deskin et al.

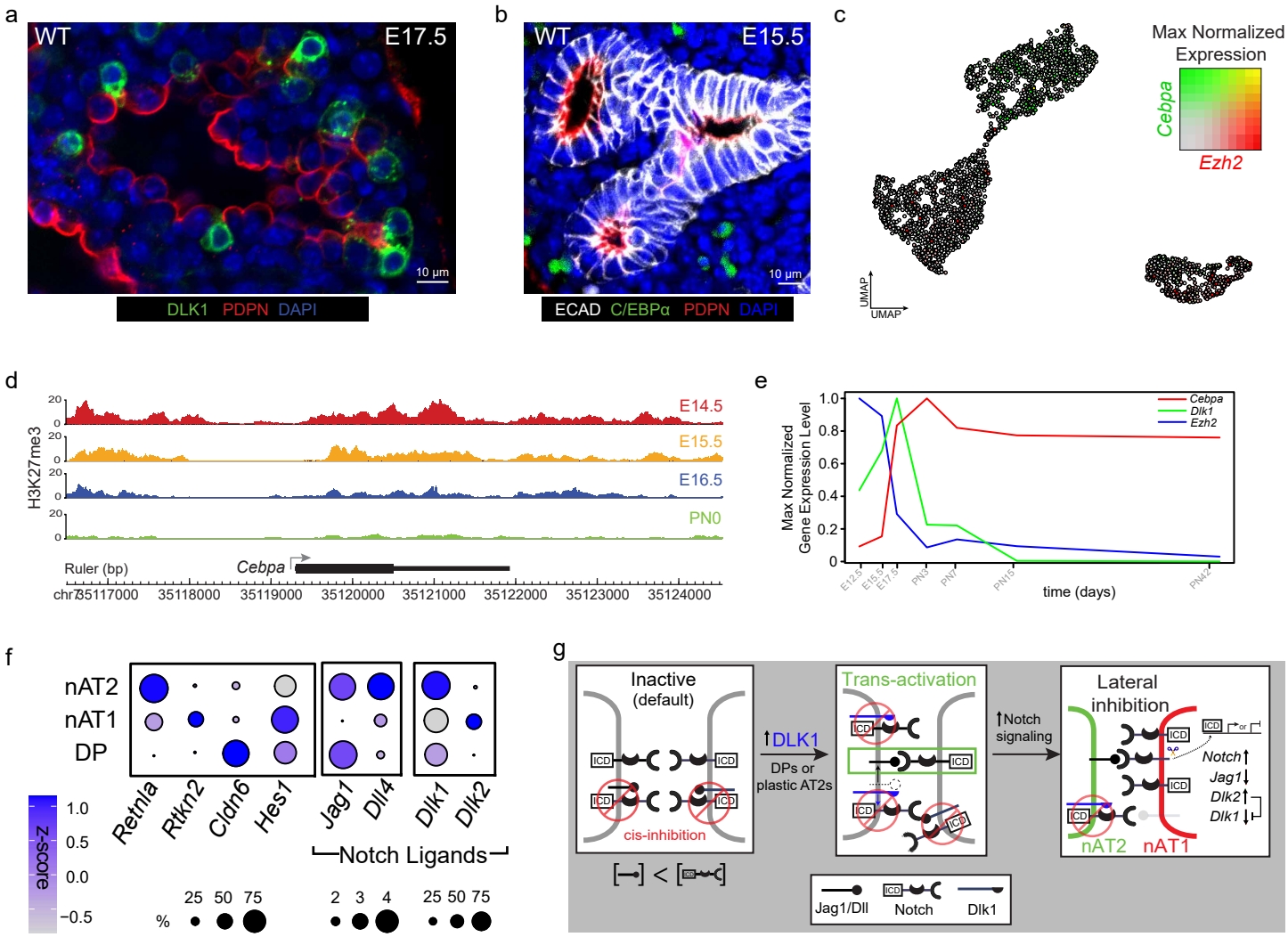
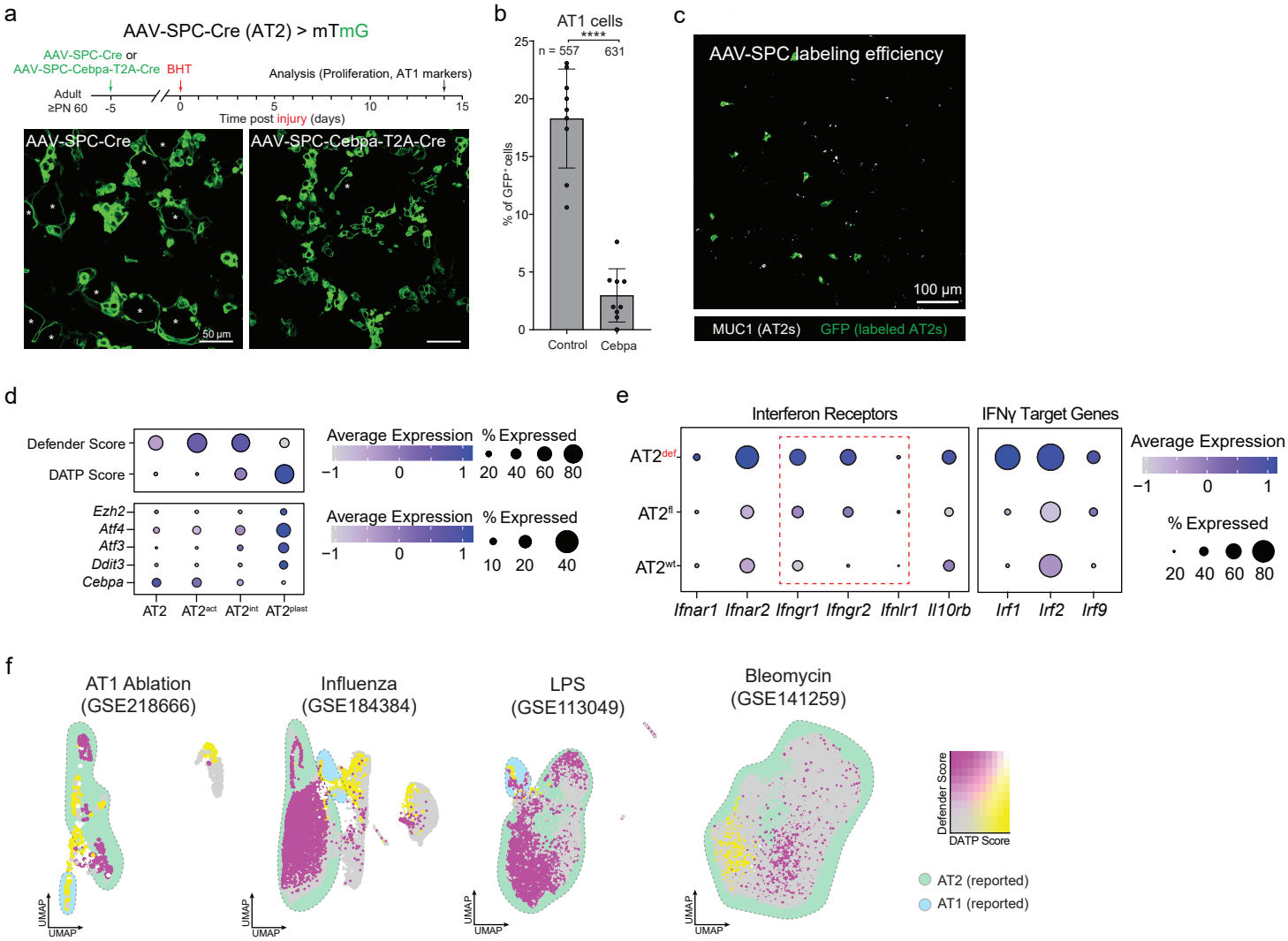
Supplementary Figure 7, Sawhney-Deskin et al.